J. Fluid Mech. (2008), *vol.* 615, *pp.* 1–25. © 2008 Cambridge University Press
doi:10.1017/S0022112008003340 Printed in the United Kingdom

The tidally induced bottom boundary layer in a rotating frame: similarity of turbulence

KEI SAKAMOTO[1,2] AND KAZUNORI AKITOMO[3]

[1]Oceanographic Research Department, Meteorological Research Institute, Tsukuba, Japan
[2]Center for Climate System Research, University of Tokyo, Kashiwa, Japan
[3]Department of Geophysics, Graduate School of Science, Kyoto University, Kyoto, Japan

(Received 13 September 2007 and in revised form 2 July 2008)

To investigate turbulent properties of the tidally induced bottom boundary layer (TBBL) in a rotating frame, we performed three-dimensional numerical experiments under unstratified conditions, varying the temporal Rossby number $Ro_t = |\sigma^*/f^*|$, where σ^* and f^* are the tidal frequency and the Coriolis parameter, respectively. The vertical profiles of the time-averaged currents and stresses showed good similarity and coincided well with the turbulent Ekman layer, when they were normalized by the modified 'outer' scales, the frictional velocity u_τ^*, $T^* = 1/|f^* + \sigma^*|$ and $\delta^* = u_\tau^*/|f^* + \sigma^*|$ for the velocity, time and length scales (σ^* is positive when the tidal ellipse rotates anticlockwise). This means that the similarity in turbulent statistics is universally applicable to the TBBL in the world's ocean except near the equator. Although strong inertial waves contaminated the perturbation field when $Ro_t \sim 1$ and masked the similarity, the apparent diffusivity κ_{ap}^* estimated by tracer experiments again showed similarity, since the inertial waves did not affect the mixing process in the present experiments. Thus, κ_{ap}^* can be represented in terms of the three external parameters: the latitude (f^*), the tidal frequency (σ^*) and the tidal amplitude (u_τ^*). The obtained scaling of $u_\tau^* \delta^* = u_\tau^{*2}/|f^* + \sigma^*|$ for κ_{ap}^* suggests that effective mixing may occur when $Ro_t \sim 1$, i.e. near the critical latitude.

1. Introduction

Dense water formed over the polar shelves due to strong surface cooling sinks and flows in benthic plumes over the continental shelf and slope, reaching the deep polar basins (Muench & Gordon 1995; Gordon 1998; Orsi, Johnson & Bullister 1999). After escaping the polar basins, it is eventually transported through the global deep basins as part of the thermohaline circulation, affecting global oceanic circulation and long-term climate change (Schmitz 1995). Properties of the dense water are modified through mixing with surrounding waters during its transport from the continental shelf to the deep basin (Foster & Carmack 1976; Fahrbach *et al.* 1995, 2001; Jacobs 2004). Tidally induced mixing is a prominent candidate for this transformation (e.g. Foster, Foldvik & Middleton 1987; Pereira, Beckmann & Hellmer 2002), since they are dominant phenomena in polar shelf regions, e.g. semidiurnal tidal currents in the Weddell shelf sea and diurnal tidal currents in the Ross shelf sea (Foldvik, Middleton & Foster 1990; Robertson, Padman & Egbert 1998). Another reason for the dominant role of tidal currents in mixing processes in polar oceans is that the tidally induced bottom boundary layer (TBBL) becomes much thicker when the semidiurnal tidal period is closer to the inertial period (Nøst 1994; Furevik & Foldvik 1996; Robertson 2001*a*, *b*; Makinson, Schröder & Østerhus 2006).

Many studies to date have analytically investigated the turbulent TBBL under the effects of the Earth's rotation (e.g. Prandle 1982; Craig 1989). When constant eddy viscosity ν^* is assumed, the vertical scale of the TBBL, $H^*_{\rm tide}$, is given by

$$H^*_{\rm tide} = \sqrt{\frac{2\nu^*}{|f^* + \sigma^*|}}, \tag{1.1}$$

where f^* is the Coriolis parameter and σ^* the tidal frequency, and an asterisk denotes a dimensional quantity. The frequency σ^* is positive (negative) when the tidal ellipse rotates anticlockwise (clockwise). Without the constraint of terrain, the tidal ellipse tends to rotate anticlockwise (clockwise) in the Southern (Northern) hemisphere due to the Coriolis effect. Therefore, f^* and σ^* have opposite signs, and $H^*_{\rm tide}$ becomes large as $|f^*|$ approaches $|\sigma^*|$. Indeed, a thick TBBL of several hundreds of metres has been observed on continental shelves in polar oceans near the M2 critical latitude (74.5°) where $|f^*|$ is equal to $|\sigma^*|$ (Foster *et al.* 1987; Furevik & Foldvik 1996; Makinson *et al.* 2006). This means that shear instability may cause effective turbulent mixing over the thick TBBL (Pereira *et al.* 2002). Sakamoto & Akitomo (2006) showed that the thick TBBL allows shear instability to be excited by weak tidal currents. However, most previous studies were based on the assumption that eddy viscosity is constant, as in laminar flow, or prescribed from turbulent theory. Few studies have been performed on the turbulent TBBL under the effects of the Earth's rotation (Aelbrecht, D'Hieres & Renouard 1999).

In contrast, many studies have provided basic knowledge of the turbulent boundary layer for either rotation or oscillation (tide), i.e. the Ekman and Stokes boundary layers, respectively (Faller & Kaylor 1966; Csanady 1967; Spalart 1989; Coleman, Ferziger & Spalart 1990, 1992; Akhavan, Kamm & Shapiro 1991*a*, *b*; Zikanov, Slinn & Dhanak 2003; Costamagna, Vittori & Blondeaux 2003). With regard to the bottom Ekman layer, Tennekes & Lumley (1972) and Coleman (1999) showed that vertical profiles of turbulent statistics such as the mean currents and stresses have similarity over wide range of the Reynolds number ($400 < Re < 350\,000$) when they are normalized by the 'outer' scales such as the frictional velocity u^*_τ, the inertial period $1/|f^*|$ and length scale $u^*_\tau/|f^*|$. The thickness of the turbulent Ekman layer is thus characterized by $u^*_\tau/|f^*|$ rather than $\sqrt{2\nu^*/|f^*|}$. With regard to the turbulent Stokes layer, Grant & Madsen (1986) obtained a similar result that the vertical scale of the boundary layer is given by $u^*_\tau/|\sigma^*|$ rather than $\sqrt{2\nu^*/|\sigma^*|}$, though the structure of the layer is different from that of the turbulent Ekman layer. Thus, properties of the turbulent TBBL under the effect of the Earth's rotation are expected to be different from those of laminar ones.

The purpose of this study is to investigate properties of the turbulent TBBL in the rotating frame. To comprehensively understand properties of the turbulent boundary layer under the two effects of oscillation and the Earth's rotation and its mixing effects, we performed numerical experiments varying the temporal Rossby number $Ro_t = |\sigma^*/f^*|$, which is an index of the relative importance of these two effects. In this paper, as a first step, we performed experiments in an unstratified fluid using a direct numerical simulation (DNS) to focus on the basic effects of oscillation and the Earth's rotation.

2. Numerical model

2.1. *Governing equations, boundary conditions and background tidal flow*

Numerical experiments were performed in a rectangular basin as shown in figure 1. The coordinate system $\boldsymbol{x} = (x, y, z)$ was set so that the z-axis is directed upward. In

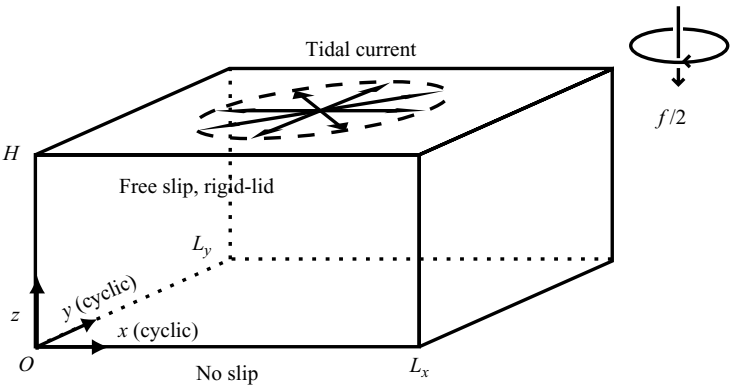

FIGURE 1. Model basin and the coordinate system with boundary conditions.

this study, instead of sea surface elevation the background tidal currents were used as the forcing of turbulent flow after Akhavan *et al.* (1991 *b*), to focus on the turbulent boundary layer induced by the tidal currents, not the tidal current itself. As described later, the background currents are horizontally uniform with the frequency of σ^* and the amplitude of U^*_{tide}.

The governing equations are the Navier–Stokes equation in the rotating frame under the rigid-lid approximation and the continuity equation for an incompressible fluid. In a non-dimensional form, the governing equations are

$$\frac{\partial \hat{\boldsymbol{u}}}{\partial t} + (\hat{\boldsymbol{u}} \cdot \nabla)\hat{\boldsymbol{u}} + \frac{1}{Ro}\boldsymbol{z} \times \hat{\boldsymbol{u}} = -\nabla \hat{p} + \frac{1}{Re}\nabla^2 \hat{\boldsymbol{u}}, \tag{2.1a}$$

$$\nabla \cdot \hat{\boldsymbol{u}} = 0, \tag{2.1b}$$

where t, $\hat{\boldsymbol{u}} = (\hat{u}, \hat{v}, \hat{w})$ and $\hat{p}$ are the non-dimensional time, velocity vector and pressure, respectively, and the non-dimensionalization used is

$$\boldsymbol{x} = \boldsymbol{x}^*/H^*_{\mathrm{tide}}, \quad t = t^*/\left(H^*_{\mathrm{tide}}/U^*_{\mathrm{tide}}\right), \quad \hat{\boldsymbol{u}} = \hat{\boldsymbol{u}}^*/U^*_{\mathrm{tide}}, \quad \hat{p} = \hat{p}^*/\left(\rho^*_0 {U^*_{\mathrm{tide}}}^2\right), \tag{2.2}$$

where ρ^*_0 is the standard density. The vector $\boldsymbol{z}$ in (2.1*a*) is the unit vector in the z-direction, and the Reynolds number Re and the Rossby number Ro are given by

$$Re = \frac{H^*_{\mathrm{tide}} U^*_{\mathrm{tide}}}{\nu^*}, \tag{2.3a}$$

$$Ro = \frac{U^*_{\mathrm{tide}}}{f^* H^*_{\mathrm{tide}}}, \tag{2.3b}$$

where f^* and ν^* are the Coriolis parameter (negative for the Southern hemisphere) and the viscosity, respectively.

Although it has been reported that the horizontal component of the Earth's rotation affects the turbulent statistics of the Ekman layer to some extent (e.g. Coleman *et al.* 1990), we did not take it into account (see (2.1*a*)). Since the flow direction rotates 360° in one tidal period, the horizontal component of the Earth's rotation has little influence on the TBBL for the time-averaged turbulent statistics (see Appendix A for details).

In (2.1*a*) and (2.1*b*), $\hat{\boldsymbol{u}}$ and $\hat{p}$ represent the sums of the background tidal components, $\boldsymbol{u}_{\mathrm{tide}} = (u_{\mathrm{tide}}, v_{\mathrm{tide}}, 0)$ and p_{tide}, and the deviations, $\boldsymbol{u}$ and p, that is,

$$\hat{\boldsymbol{u}} = \boldsymbol{u}_{\mathrm{tide}} + \boldsymbol{u}, \quad \hat{p} = p_{\mathrm{tide}} + p. \tag{2.4}$$

The background components, $\boldsymbol{u}_{\rm tide}$ and $p_{\rm tide}$, satisfy the linear Navier–Stokes equation and the continuity equation,

$$\frac{\partial \boldsymbol{u}_{\rm tide}}{\partial t} + \frac{1}{Ro} z \times \boldsymbol{u}_{\rm tide} = -\nabla p_{\rm tide} + \frac{1}{Re}\frac{\partial^2 \boldsymbol{u}_{\rm tide}}{\partial z^2}, \tag{2.5a}$$

$$\nabla \cdot \boldsymbol{u}_{\rm tide} = 0, \tag{2.5b}$$

and then the equations for $\boldsymbol{u}$ and p are derived by subtracting (2.5a) and (2.5b) from (2.1a) and (2.1b), respectively,

$$\frac{\partial \boldsymbol{u}}{\partial t} + (\boldsymbol{u}_{\rm tide}\cdot\nabla)\boldsymbol{u} + (\boldsymbol{u}\cdot\nabla)\boldsymbol{u}_{\rm tide} + (\boldsymbol{u}\cdot\nabla)\boldsymbol{u} + \frac{1}{Ro} z \times \boldsymbol{u} = -\nabla p + \frac{1}{Re}\nabla^2 \boldsymbol{u}, \tag{2.6a}$$

$$\nabla \cdot \boldsymbol{u} = 0. \tag{2.6b}$$

The background current $\boldsymbol{u}_{\rm tide}$ has been analytically obtained in previous studies with the no-slip bottom and free-slip surface conditions (e.g. Soulsby 1983). Assuming the temporally oscillating pressure gradient in the x-direction $\partial p_{\rm tide}/\partial x$ (which is equivalent to inclination of the surface elevation), $\boldsymbol{u}_{\rm tide}$ is given as follows:

$$\begin{aligned} & u_{\rm tide}(z,t) + {\rm i} v_{\rm tide}(z,t) \\ & = \begin{cases} \dfrac{Ro_t+1}{2}{\rm e}^{{\rm i}|Ro|Ro_t t}(1-\exp(-(1-{\rm i})z))) \\ \quad + \dfrac{Ro_t-1}{2}{\rm e}^{-{\rm i}|Ro|Ro_t t}\left(1-\exp\left(-(1+{\rm i})\sqrt{\left|\dfrac{Ro_t-1}{Ro_t+1}\right|}z\right)\right) & \text{for } Ro_t < 1 \\ \dfrac{Ro_t+1}{2Ro_t}{\rm e}^{{\rm i}|Ro|Ro_t t}(1-\exp(-(1+{\rm i})z))) \\ \quad + \dfrac{Ro_t-1}{2Ro_t}{\rm e}^{-{\rm i}|Ro|Ro_t t}\left(1-\exp\left(-(1+{\rm i})\sqrt{\left|\dfrac{Ro_t-1}{Ro_t+1}\right|}z\right)\right) & \text{for } Ro_t > 1, \end{cases} \end{aligned} \tag{2.7}$$

where $Ro_t (= |\sigma^*/f^*|)$ is the temporal Rossby number (see Appendix A in Sakamoto & Akitomo 2006 for a detailed derivation). Since $\boldsymbol{u}_{\rm tide}$ was derived under a constant viscosity, it has the same vertical structure as in laminar oscillating flow.

For the deviation $\boldsymbol{u}$, the no-slip condition was imposed at the bottom ($z = 0$), and the free-slip one at the rigid sea surface ($z = H$),

$$u = v = w = 0 \qquad \text{at} \quad z = 0, \tag{2.8a}$$

$$\frac{\partial u}{\partial z} = \frac{\partial v}{\partial z} = w = 0 \qquad \text{at} \quad z = H, \tag{2.8b}$$

and the periodic condition was imposed at the horizontal boundaries ($x = 0, L_x$ and $y = 0, L_y$).

Although three parameters (Ro, Re and Ro_t) appear in (2.6a), (2.6b) and (2.7), only two are independent since Ro is related to Re and Ro_t by

$$Ro = {\rm sgn}(f^*)\frac{Re|1+{\rm sgn}(f^*\sigma^*)Ro_t|}{2}, \tag{2.9}$$

where ${\rm sgn}(A)$ is the sign function which represents the sign of A. Equation (2.9) reduces to $Ro = -Re|1-Ro_t|/2$ for our settings of $f^* < 0$ and $\sigma^* > 0$.

2.2. *Experimental cases*

Six cases, A to F, were considered, varying Ro_t from 0.5 to 2.0, with two additional cases of a steady Ekman flow (case Ek, $Ro_t = 0$) and a Stokes flow (St, $Ro_t = \infty$)

Case	Ek	A	B	C	D	E	F	St
$Ro_t(=\lvert\sigma^*/f^*\rvert)$	0	0.5	0.8	0.95	1.05	1.2	2.0	∞
$Re(=H^*_{\rm tide}U^*_{\rm tide}/\nu^*)$	1000	1000	2000	4350	4580	2450	1410	1000
$Ro(=U^*_{\rm tide}/(f^*H^*_{\rm tide}))$	-500	-250	-200	-109	-115	-246	-705	$-\infty$
$u_\tau(=u^*_\tau/U^*_{\rm tide})$	0.0539	0.0443	0.0446	0.0389	0.0374	0.0417	0.0409	0.0350
$T(=T^*/(H^*_{\rm tide}/U^*_{\rm tide}))$	500	500	1000	2180	2290	1230	705	500
$\delta(=\delta^*/H^*_{\rm tide})$	27.0	22.2	44.6	84.9	85.5	51.1	28.8	17.5

TABLE 1. Non-dimensional parameters and the outer scales.

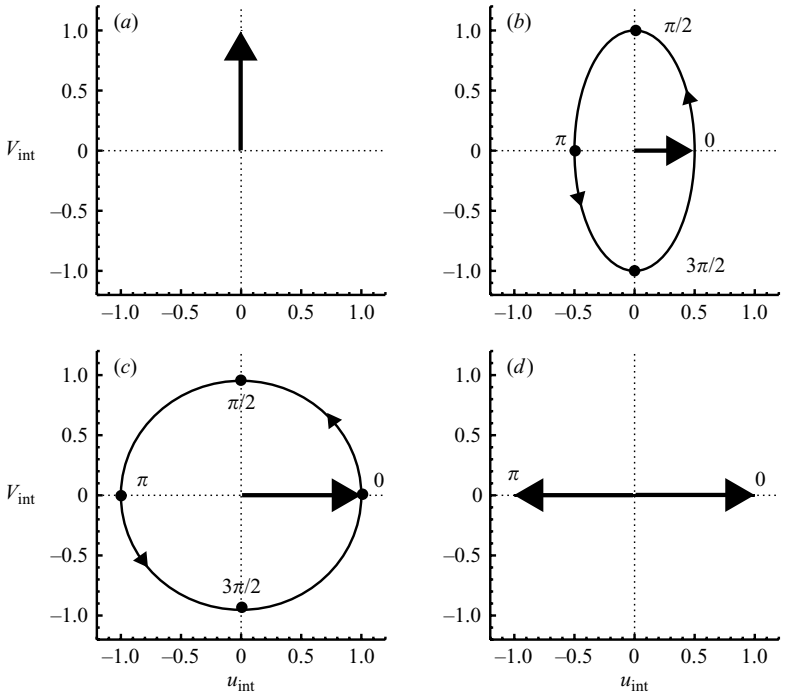

FIGURE 2. The tidal ellipse in the interior region $\boldsymbol{u}_{\rm int}$ for cases (*a*) Ek, (*b*) A, (*c*) D and (*d*) St. The arrows on the ellipse in (*b*) and (*c*) indicate the direction of rotation.

(table 1). Substitution of (1.1) into (2.3*a*) and some rearrangement yield

$$Re = \frac{U^*_{\rm tide}}{\sqrt{\nu^*|\sigma^*|}}\sqrt{\frac{2Ro_t}{|1+{\rm sgn}(f^*\sigma^*)Ro_t|}}, \tag{2.10}$$

so that Re is depends on Ro_t when $U^*_{\rm tide}$, σ^* and ν^* are set constant. Due to limited computational resources, the Re values ranging from 1000 to 4500 for the experiments are rather small compared to the real oceans ($Re = 10^5 \sim 10^6$). However, fundamental properties of the turbulent TBBL can be obtained, because it was shown by Coleman (1999) that basic properties of turbulent boundary layers such as mean currents and stresses become approximately independent of Re when Re exceeds 10^3.

Differences in the background tidal current $\boldsymbol{u}_{\rm tide}$ among cases are seen in the tidal ellipse which is defined by the stress-free interior current $\boldsymbol{u}_{\rm int}$ (figure 2),

$$\boldsymbol{u}_{\rm int}(t) = \lim_{z\to\infty}\boldsymbol{u}_{\rm tide}(z,t). \tag{2.11}$$

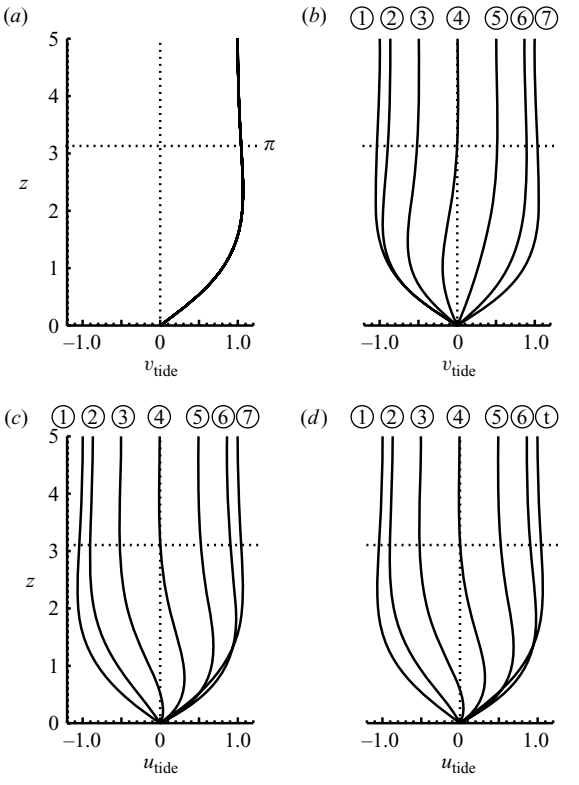

FIGURE 3. Vertical profiles of the major-axis component of the background tidal currents, i.e. v_{tide} for case (*a*) Ek and (*b*) A, and u_{tide} for (*c*) D and (*d*) St. The currents evolve from the left profile to the right every $\pi/6$ tidal phase. The horizontal dotted lines indicate $z = \pi$. The vertical range of $0 < z < 5$ is shown, since $\boldsymbol{u}_{\mathrm{tide}}$ hardly changes in $5 < z < H = 256$.

Although the pressure gradient is in the x-direction, the tidal ellipse has an anticlockwise rotation, and its ellipticity is equivalent to Ro_t for cases A to F. Under the same pressure gradient, $\boldsymbol{u}_{\mathrm{int}}$ is unidirectional in the y-direction for case Ek, and bidirectional in the x-direction for case St. The current shear extends from the bottom to $z = \pi$ in all cases (figure 3), and then the TBBL is scaled well by H^*_{tide} (e.g. Soulsby 1983; Craig 1989).

2.3. *Numerical settings*

The horizontal size of the domain, L_x and L_y, is 64, while the depth H is 256 after Coleman (1999) who studied the turbulent Ekman layer. The horizontal grid intervals, Δx and Δy, are 0.125 (512 cells) and the vertical one, Δz, changes from 0.02 near the bottom to 10 in the interior (160 cells). These settings of the model were adequate to represent universal turbulent characteristics reported by previous studies on turbulent boundary layers (Appendix B). It was also confirmed that the turbulent statistics hardly changed when the domain size was doubled case D with the highest Re (the differences in the frictional velocity and the direction of the bottom stress vector were 0.3% and 0.4°, respectively).

Time integration was carried out over 12 tidal cycles after small perturbations were imposed on the velocity field to trigger instability. Cases C and D, however, had a longer preliminary integration (40 cycles) using a coarse-resolution model ($\Delta x =$

$\Delta y = 0.5$, $\Delta z = 0.1$ to 20) before the main experiments, since a longer time was needed for the quasi-steady states to be established. The method of numerical integration of the governing equations was the same as in Akitomo (1999). Spatial finite differencing was implemented on the staggered grid system and a leap-frog scheme was used for time-differencing (Matsuno 1966). The case Ek clearly reproduced the turbulent Ekman layer with $Re = 1000$ obtained by Coleman (1999): the differences in the frictional velocity and the direction of the bottom stress vector were 0.07% and 0.1°, respectively. Agreement was also found in the vertical profiles of the mean currents and stresses.

2.4. *Averaging operators*

We define some averaging operators for analysis of experimental results in the following sections. First, the horizontal averaging, $\overline{\mathscr{F}}^{x,y}$, is defined by

$$\overline{\mathscr{F}}^{x,y}(z,t) = \frac{1}{L_x L_y}\int_0^{L_x}\int_0^{L_y} \mathscr{F}(x,y,z,t)\,\mathrm{d}y\,\mathrm{d}x. \tag{2.12}$$

The time averaging $\overline{\mathscr{F}}^{t}$ is estimated from the m to n tidal cycle after the start of the experiments, that is,

$$\overline{\mathscr{F}}^{t}(x,y,z) = \frac{1}{(n-m)\times 2\pi/(|Ro|Ro_t)}\int_{m\times 2\pi/(|Ro|Ro_t)}^{n\times 2\pi/(|Ro|Ro_t)} \mathscr{F}(x,y,z,t)\,\mathrm{d}t, \tag{2.13}$$

where $2\pi/(|Ro|Ro_t) = (2\pi/\sigma^*)/(H^*_{\mathrm{tide}}/U^*_{\mathrm{tide}})$ is the non-dimensional tidal period. As mentioned later, $(m,n) = (2,12)$ in this study.

3. Results

3.1. *Transition to turbulence*

The boundary layer was unstable in all cases. Features of the instabilities agree with the result of Sakamoto & Akitomo (2006). Perturbations grew quickly after the start of the experiment, and the flows transitioned to turbulence within one tidal cycle. After two tidal cycles, the area-averaged kinetic energy of turbulent motion showed a regular oscillation with half the tidal period and exhibited no one-way trend. Thus, we used data of 10 tidal cycles, from cycles 2 to 12, for the following analysis. The time t is counted by tidal cycle in the following for convenience.

Figure 4 shows the eddy kinetic energy E on an x–z section at the end of the experiments for cases A and D. The energy E is defined as

$$E = \tfrac{1}{2}(u'^2 + v'^2 + w'^2), \tag{3.1}$$

where the perturbation velocity $(u', v', w') = (u - \overline{u}^{x,y}, v - \overline{v}^{x,y}, w)$. In both cases, the flow was highly irregular, and perturbations were vigorous especially near the bottom boundary as seen in the horizontal averaged $\overline{E}^{x,y}$. The region of $E > 10^{-4}$ was confined to $z < 20$ in case A, but it extended to the upper boundary at $z = 256$ in case D. This indicates that the non-dimensional vertical scale of the turbulent TBBL changes depending on Ro_t, unlike the 'laminar' TBBL (e.g. figure 3).

3.2. *Time-averaged currents and stresses*

First, we investigated the time-averaged currents in the TBBL relative to the interior flow (velocity defect), in the same manner as previous studies (Coles 1956; Tennekes & Lumley 1972; Coleman 1999). The velocity defect $\boldsymbol{u}_{\mathrm{def}}$ is defined as the difference

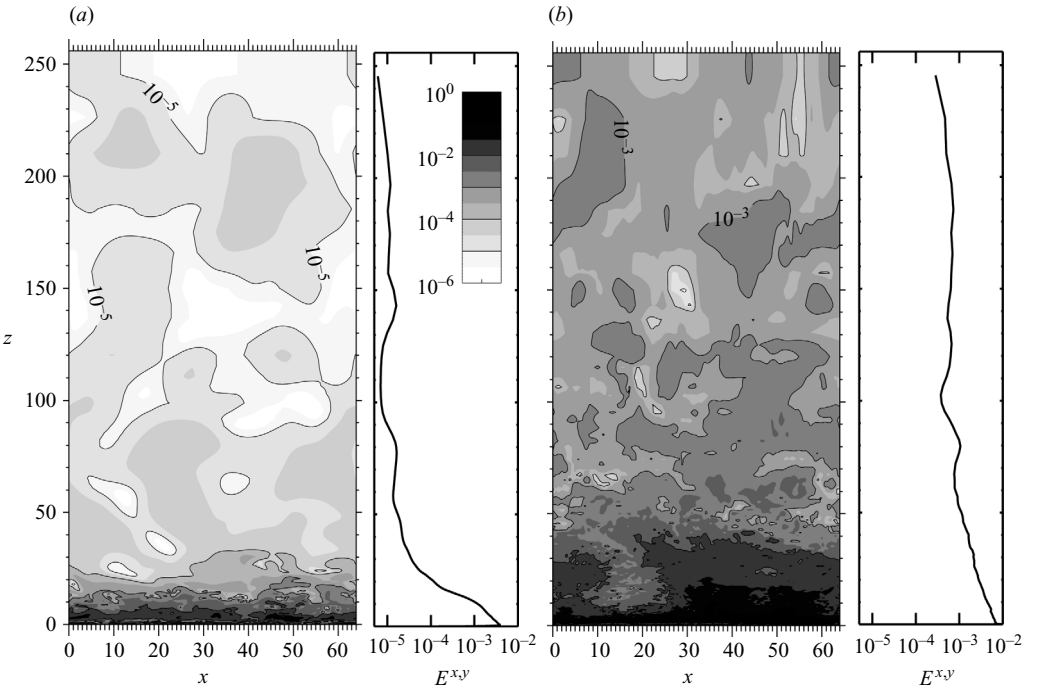

FIGURE 4. Instantaneous field of the eddy kinetic energy $E = (u'^2 + v'^2 + w'^2)/2$ at the vertical section at $y = 0$ together with the horizontal averaged $\overline{E}^{x,y}$ at $t = 12$ (12 tidal cycles) of (a) case A and (b) case D. Contour interval is 10^{-1}, and darker shades represent larger values.

between the total flow $\hat{\boldsymbol{u}} = \boldsymbol{u} + \boldsymbol{u}_{\mathrm{tide}}$ and the interior flow $\boldsymbol{u}_{\mathrm{int}}$, that is,

$$\boldsymbol{u}_{\mathrm{def}}(x, y, z, t) = \hat{\boldsymbol{u}}(x, y, z, t) - \boldsymbol{u}_{\mathrm{int}}(t) = \boldsymbol{u}(x, y, z, t) + \boldsymbol{u}_{\mathrm{tide}}(z, t) - \boldsymbol{u}_{\mathrm{int}}(t). \tag{3.2}$$

Thus, its horizontal average is given by

$$\overline{\boldsymbol{u}_{\mathrm{def}}}^{x,y}(z, t) = \overline{\hat{\boldsymbol{u}}}^{x,y}(z, t) - \boldsymbol{u}_{\mathrm{int}}(t) = \overline{\boldsymbol{u}}^{x,y}(z, t) + \boldsymbol{u}_{\mathrm{tide}}(z, t) - \boldsymbol{u}_{\mathrm{int}}(t). \tag{3.3}$$

As seen in figure 5(a), the total flow $\overline{\hat{\boldsymbol{u}}}^{x,y}$ changes direction and magnitude following the interior flow $\boldsymbol{u}_{\mathrm{int}}$.

To discuss the basic structure of the velocity defect $\overline{\boldsymbol{u}_{\mathrm{def}}}^{x,y}$, we introduce a new coordinate system rotating with $\boldsymbol{u}_{\mathrm{int}}$. In these new coordinates, the horizontal vector $\boldsymbol{a} = (a, b)$ is

$$\langle \boldsymbol{a} \rangle_{\mathrm{int}} = [a', b']_{\mathrm{int}} = [a\cos\theta_{\mathrm{int}} + b\sin\theta_{\mathrm{int}}, -a\sin\theta_{\mathrm{int}} + b\cos\theta_{\mathrm{int}}]_{\mathrm{int}}, \tag{3.4}$$

where $\theta_{\mathrm{int}}(t)$ is the azimuthal angle of $\boldsymbol{u}_{\mathrm{int}}$ (figure 5b). The notations $\langle\ \ \rangle_{\mathrm{int}}$ and $[\ ,\ ]_{\mathrm{int}}$ indicate a vector and components in the new coordinates, respectively, and the first (second) component of $[\ ,\ ]_{\mathrm{int}}$ denotes the component parallel with (normal to) $\boldsymbol{u}_{\mathrm{int}}$. Converting (3.3) into this coordinate and averaging temporally yields

$$\begin{aligned}
\overline{\langle \overline{\boldsymbol{u}_{\mathrm{def}}}^{x,y} \rangle_{\mathrm{int}}}^{t}(z) &= \overline{\langle \overline{\boldsymbol{u}}^{x,y} \rangle_{\mathrm{int}}}^{t} + \overline{\langle \boldsymbol{u}_{\mathrm{tide}} \rangle_{\mathrm{int}}}^{t} - \overline{\langle \boldsymbol{u}_{\mathrm{int}} \rangle_{\mathrm{int}}}^{t} \\
&= \left[\overline{u_{\mathrm{def}}}^{x,y,t}, \overline{v_{\mathrm{def}}}^{x,y,t} \right]_{\mathrm{int}} \\
&= \Big[\overline{(\overline{u}^{x,y} + u_{\mathrm{tide}})\cos\theta_{\mathrm{int}} + (\overline{v}^{x,y} + v_{\mathrm{tide}})\sin\theta_{\mathrm{int}}}^{t} - \overline{|\boldsymbol{u}_{\mathrm{int}}|}^{t}, \\
&\quad \overline{-(\overline{u}^{x,y} + u_{\mathrm{tide}})\sin\theta_{\mathrm{int}} + (\overline{v}^{x,y} + v_{\mathrm{tide}})\cos\theta_{\mathrm{int}}}^{t} \Big]_{\mathrm{int}}.
\end{aligned} \tag{3.5}$$

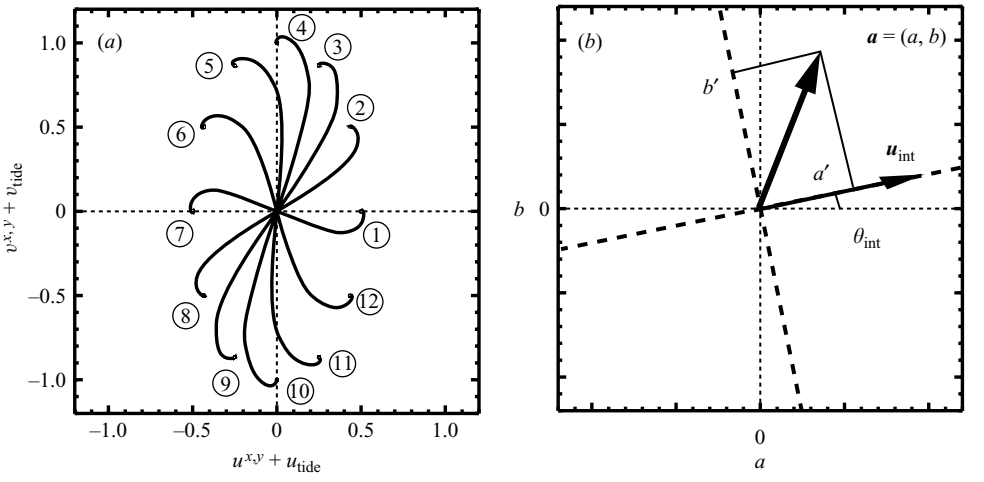

FIGURE 5. (*a*) Time evolution of a hodograph of the total velocity $\overline{\tilde{\boldsymbol{u}}}^{x,y} = \overline{\boldsymbol{u}}^{x,y} + \boldsymbol{u}_{\rm tide}$ every $\pi/6$ phase for case A. The numbers on the hodographs show the order of time evolution during the 12th tidal cycle. (*b*) Schematic diagram of coordinate conversion of the vector $\boldsymbol{a} = (a, b)$ in the fixed system (the axes are indicated by the dotted lines) to $\langle \boldsymbol{a} \rangle_{\rm int} = [a', b']_{\rm int}$ in the system rotating with $\boldsymbol{u}_{\rm int}$ (the axes are the dashed lines).

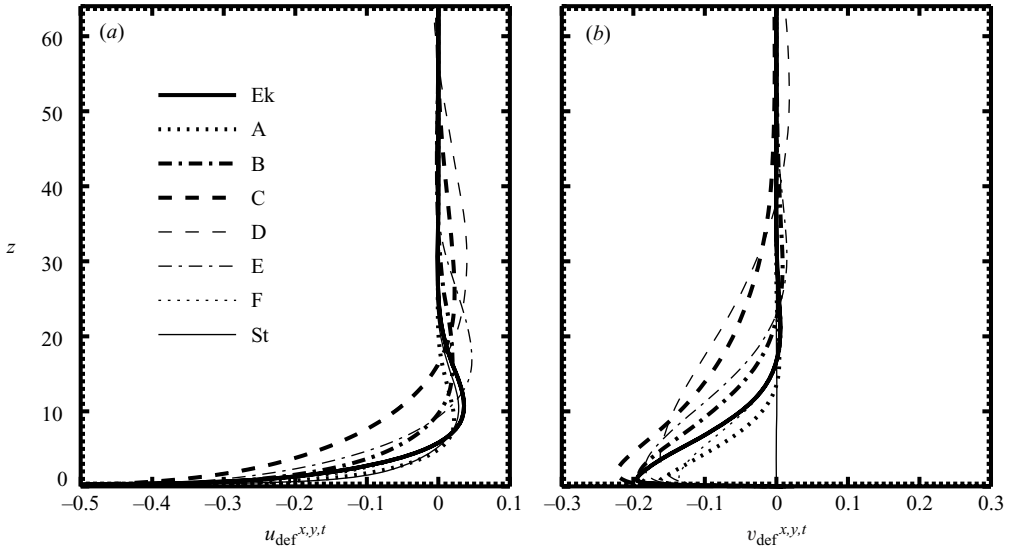

FIGURE 6. Vertical profiles of the time-averaged velocity defects, (*a*) $\overline{u_{\rm def}}^{x,y,t}$ and (*b*) $\overline{v_{\rm def}}^{x,y,t}$ for all eight cases. The profiles for cases D, E and F in (*b*) are shown with changed sign (i.e. $-\overline{v_{\rm def}}^{x,y,t}$ instead of $\overline{v_{\rm def}}^{x,y,t}$) for the sake of comparison. Only the vertical range of $0 < z < 64$ is shown.

Figure 6 shows vertical profiles of the parallel and normal components $\overline{u_{\rm def}}^{x,y,t}$ and $\overline{v_{\rm def}}^{x,y,t}$ in (3.5) for all cases. Starting with negative values near the bottom, $\overline{u_{\rm def}}^{x,y,t}$ increased to become positive at the middle levels, and converged to zero in the upper region. Note that the height at which $\overline{u_{\rm def}}^{x,y,t}$ vanishes increased as Ro_t approaches unity: $z \sim 20$ for cases A and F, $z \sim 30$ for B and E, and $z \sim 50$ for C and D. A similar dependence on Ro_t was found for $\overline{v_{\rm def}}^{x,y,t}$. This means that the velocity defect

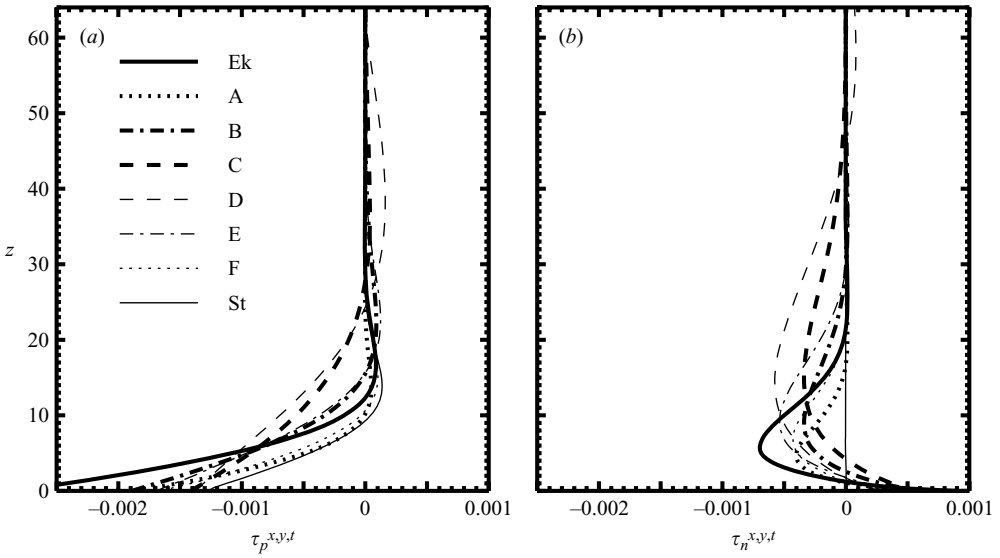

FIGURE 7. As figure 6, but for the time-averaged stresses, (*a*) $\overline{\tau_p}^{x,y,t}$ and (*b*) $\overline{\tau_n}^{x,y,t}$.

cannot be scaled by H^*_{tide} in the turbulent state. This is in contrast to the 'laminar' tidal currents or the tidal currents with a constant eddy viscosity, where the vertical shear is confined to $z < \pi$ regardless of Ro_t (e.g. figure 3).

The velocity defect $\overline{\boldsymbol{u}_{\mathrm{def}}}^{x,y}$ is produced by the horizontal stress $\overline{\boldsymbol{\tau}}^{x,y}$, which is given by

$$\begin{aligned}\overline{\boldsymbol{\tau}}^{x,y} &= (\overline{\tau_x}^{x,y}, \overline{\tau_y}^{x,y}) \\ &= \left(-\overline{u'w'}^{x,y} + \frac{1}{Re}\frac{\partial}{\partial z}(\overline{u}^{x,y} + u_{\mathrm{tide}}), -\overline{v'w'}^{x,y} + \frac{1}{Re}\frac{\partial}{\partial z}(\overline{v}^{x,y} + v_{\mathrm{tide}})\right), \quad (3.6)\end{aligned}$$

and its time-average $\overline{\langle\overline{\boldsymbol{\tau}}^{x,y}\rangle_{\mathrm{int}}}^{t}$ in the coordinate system rotating with $\boldsymbol{u}_{\mathrm{int}}$ is written

$$\begin{aligned}\overline{\langle\overline{\boldsymbol{\tau}}^{x,y}\rangle_{\mathrm{int}}}^{t}(z) &= \left[\overline{\tau_p}^{x,y,t}, \overline{\tau_n}^{x,y,t}\right]_{\mathrm{int}} \\ &= \left[\overline{\overline{\tau_x}^{x,y}\cos\theta_{\mathrm{int}} + \overline{\tau_y}^{x,y}\sin\theta_{\mathrm{int}}}^{t}, \overline{-\overline{\tau_x}^{x,y}\sin\theta_{\mathrm{int}} + \overline{\tau_y}^{x,y}\cos\theta_{\mathrm{int}}}^{t}\right]_{\mathrm{int}}, \quad (3.7)\end{aligned}$$

where $\overline{\tau_p}^{x,y,t}$ and $\overline{\tau_n}^{x,y,t}$ represent the component parallel with and normal to $\boldsymbol{u}_{\mathrm{int}}$, respectively. In contrast to the laminar state, the Reynolds stress terms ($-\overline{u'w'}^{x,y}$ and $-\overline{v'w'}^{x,y}$ in (3.6)) were larger than the viscous terms ($Re^{-1}\partial(\overline{u}^{x,y} + u_{\mathrm{tide}})/\partial z$ and $Re^{-1}\partial(\overline{v}^{x,y} + v_{\mathrm{tide}})/\partial z$) in most of the water column (not shown). As seen in figure 7, the vertical profiles of $\overline{\tau_p}^{x,y,t}$ and $\overline{\tau_n}^{x,y,t}$ were different among the cases, corresponding to the shear of $\overline{u_{\mathrm{def}}}^{x,y,t}$ and $\overline{v_{\mathrm{def}}}^{x,y,t}$ (figure 6). These differences in the vertical scale of the turbulent statistics among the cases strongly suggest the need to introduce new scalings.

Studying the turbulent Ekman layer, Tennekes & Lumley (1972) and Coleman (1999) introduced the 'outer' scales, the frictional velocity u^*_τ, the inertial period $1/|f^*|$ and the length scale $u^*_\tau/|f^*|$, and found similarity in turbulent statistics. Following these studies, we introduce outer scales modified for the TBBL in the rotating frame, that is, the frictional velocity $u^*_\tau = |\overline{\langle\overline{\boldsymbol{\tau}^*}^{x,y}\rangle_{\mathrm{int}}}^{t}(0)/\rho^*_0|^{1/2}$ for velocity scale, $T^* = 1/|f^* + \sigma^*|$ for time scale and $\delta^* = u^*_\tau/|f^* + \sigma^*|$ for length scale. As far

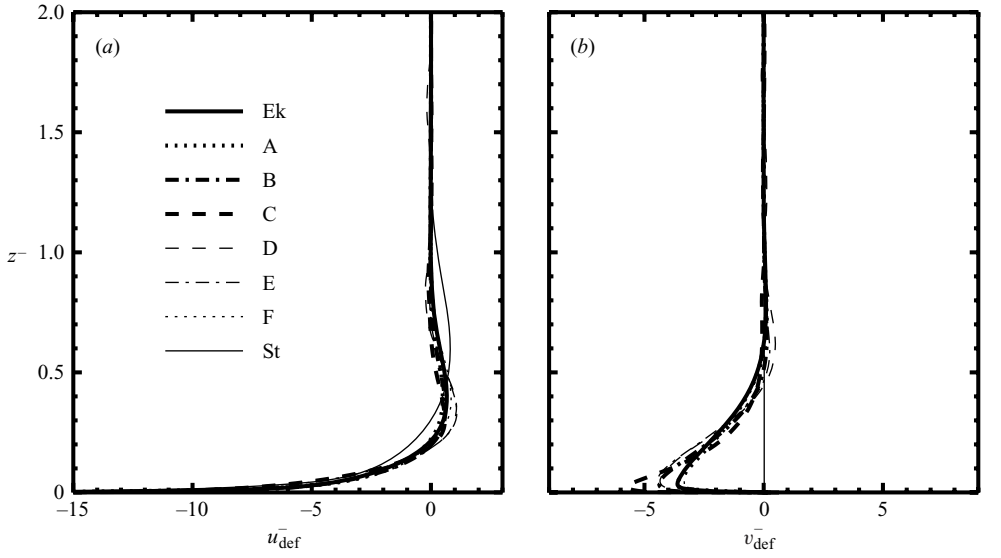

FIGURE 8. As figure 6, but normalized by the outer scales. (*a*) $u^-_{\mathrm{def}} = \overline{u_{\mathrm{def}}}^{x,y,t}/u_\tau$ and (*b*) $v^-_{\mathrm{def}} = \overline{v_{\mathrm{def}}}^{x,y,t}/u_\tau$.

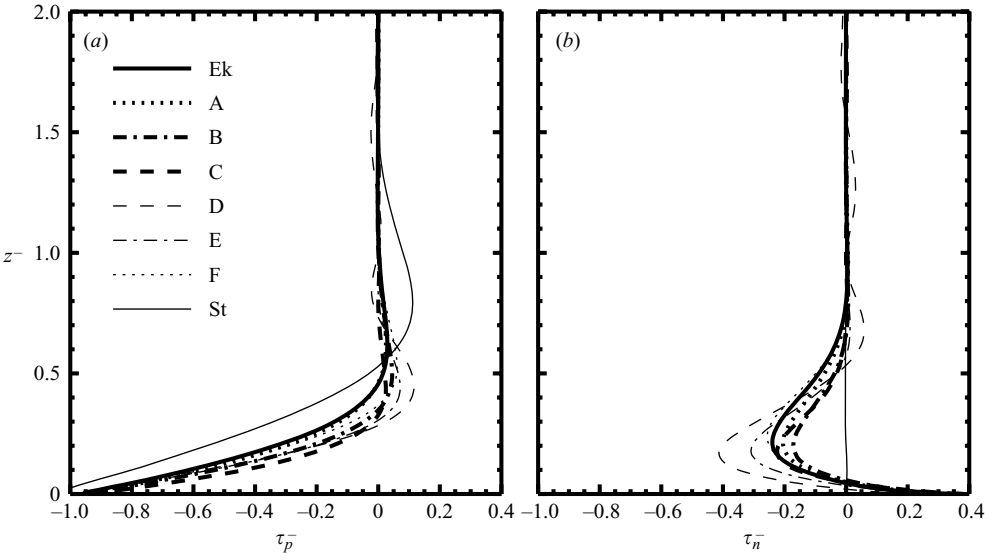

FIGURE 9. As figure 7, but normalized by the outer scales. (*a*) $\tau^-_p = \overline{\tau_p}^{x,y,t}/u^2_\tau$ and (*b*) $\tau^-_n = \overline{\tau_n}^{x,y,t}/u^2_\tau$.

as we know, it is the first time that such scales have been proposed. Table 1 in § 2 shows the ratios of the outer scales and the laminar scales, i.e. $u_\tau = u^*_\tau/U^*_{\mathrm{tide}}$, $T = T^*/(H^*_{\mathrm{tide}}/U^*_{\mathrm{tide}})$ and $\delta = \delta^*/H^*_{\mathrm{tide}}$. Although u_τ changes by about 20%, T varies significantly among the cases (factor of 4), because f^* and σ^* have opposite signs. As a result, δ exhibited a large change from 22.2 (case A) to 85.5 (case D).

Figures 8 and 9 show the time-averaged velocity defects and horizontal stresses, normalized by the outer scales, respectively, i.e. $u^-_{\mathrm{def}} = u^*_{\mathrm{def}}/u^*_\tau = \overline{u_{\mathrm{def}}}^{x,y,t}/u_\tau$ and

$v_{\mathrm{def}}^{-} = \overline{v_{\mathrm{def}}}^{x,y,t}/u_\tau$, and $\tau_p^{-} = \tau_p^*/(\rho_0(u_\tau^*)^2) = \overline{\tau_p}^{x,y,t}/u_\tau^2$ and $\tau_n^{-} = \overline{\tau_n}^{x,y,t}/u_\tau^2$. For cases A to F, the vertical profiles coincided well with those of case Ek (the thick solid lines) in both the velocity defect and the stress. The figure shows that u_{def}^{-} had a positive peak at $z^- \sim 0.3$ and decreased gradually to zero at $z^- \sim 0.7$, and v_{def}^{-} reached a negative peak at $z^- \sim 0.05$ and approached zero at $z^- \sim 0.7$; τ_p^- had a small positive peak at $z^- \sim 0.4$, τ_n^- had a negative peak at $z^- \sim 0.2$ and both τ_p^- and τ_n^- vanished at $z^- \sim 0.7$. These results mean that the same similarity as in the turbulent Ekman layer is valid for the turbulent TBBL.

This extension of similarity to the TBBL can be explained as follows. Generally, the dimensional tidal ellipse $\boldsymbol{u}_{\mathrm{int}}^*(t)$ can be represented as a sum of the anticlockwise and clockwise components as

$$\boldsymbol{u}_{\mathrm{int}}^*(t) = (R_+^* \cos(\sigma^* t^* + \theta_+) + R_-^* \cos(-\sigma^* t^* + \theta_-),\ R_+^* \sin(\sigma^* t^* + \theta_+) + R_-^* \sin(-\sigma^* t^* + \theta_-)), \quad (3.8)$$

where R_+^* (R_-^*) and θ_+ (θ_-) are the amplitude and the initial phase of the anticlockwise (clockwise) component (e.g. Makinson 2002). Each component has constant velocity (R_+^* or R_-^*) and rotates anticlockwise or clockwise with angular speed σ^*.

The boundary layer induced by the anticlockwise component, can be regarded as a steady Ekman layer with a 'modified Coriolis parameter', $f^* + \sigma^*$, by introducing a coordinate system rotating anticlockwise with speed σ^*. In the same manner, the boundary layer induced by the clockwise component can be regarded as an Ekman layer with $f^* - \sigma^*$. Since R_+^* is from 2 (cases A and F) to 40 times (C and D) larger than R_-^* in the present experiment, the anticlockwise component dominates the scales of energy-containing vortices, although coexisting anticlockwise and clockwise components cause a deviation of profiles from similarity to some extent. It follows that the turbulent TBBL can be approximated as a turbulent Ekman layer with modified Coriolis parameter $f^* + \sigma^*$. (In the Northern hemisphere, the modified Coriolis parameter is $f^* - \sigma^*$, since the tidal ellipse rotates clockwise.)

In a strict sense, the structures of the current and stress in the pure Stokes layer (case St) were different from those in cases A to F and Ek (figures 8 and 9), though the scalings were valid. This is probably because the above discussion ignoring the clockwise component is not valid for the Stokes layer, where $R_-^* = R_+^*$.

3.3. *Perturbation field*

To examine whether the same similarity as in the velocity defect and horizontal stress holds for the perturbation field, perturbation velocity and length scales, q and l, are defined by

$$q(z) = (\overline{E}^{x,y,t})^{1/2}, \quad (3.9)$$

$$l(z) = \overline{\int_{z_0}^{z_1} \frac{\overline{w(x,y,z,t)w(x,y,z',t)}^{x,y}}{\sqrt{\overline{w^2(x,y,z,t)}^{x,y}}\sqrt{\overline{w^2(x,y,z',t)}^{x,y}}} \mathrm{d}z'}^{t}, \quad (3.10)$$

where z_0 and z_1 are the heights where the correlation (the integrand of (3.10)) vanishes. Then, l corresponds to the integral length scale (Tennekes & Lumley 1972). In the experiments, the correlation dropped rapidly from unity near the reference height z, and decreased slowly to zero at z_0 and z_1 away from z. The difference between z_0 and z_1 was roughly twice l for any z.

Figure 10 shows the vertical profiles of $q^- = q/u_\tau$ and $l^- = l/\delta$ normalized by the outer scales. Although q^- and l^- appeared to have similarity for $z^- < 0.5$, a

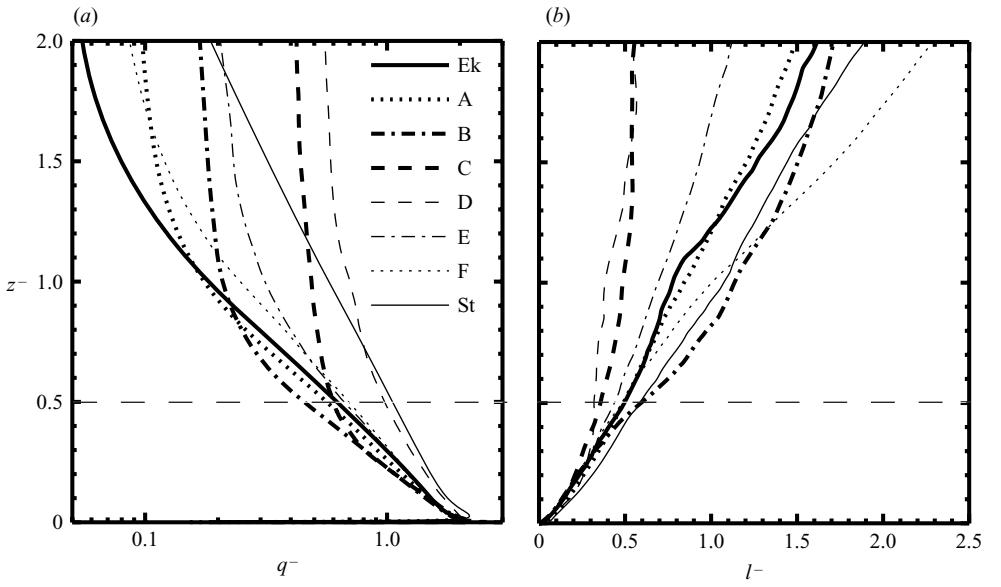

FIGURE 10. The normalized vertical profiles of (*a*) the velocity scale $q^- = q/u_\tau (= q^*/u_\tau^*)$ and (*b*) the length scale $l^- = l/\delta (= l^*/\delta^*)$ of perturbations for all the cases. The horizontal long-dashed lines indicate $z^- = 0.5$.

discrepancy appeared for $z^- > 0.5$. As Ro_t approaches unity, q^- (l^-) became larger (smaller) compared with case Ek.

To clarify the reason of the discrepancy for $z^- > 0.5$, we examined the equation for the eddy kinetic energy E, which is derived from (2.6*a*) and (2.6*b*),

$$\frac{\partial}{\partial t}\overline{E}^{x,y} = -\left\{\frac{\partial}{\partial z}(u_{\rm tide} + \overline{u}^{x,y})\overline{u'w'}^{x,y} + \frac{\partial}{\partial z}(v_{\rm tide} + \overline{v}^{x,y})\overline{v'w'}^{x,y}\right\}$$
$$-\frac{\partial}{\partial z}\left(\overline{p'w'}^{x,y} + \overline{w'E}^{x,y}\right)$$
$$-\frac{1}{Re}\left\{\overline{(\nabla u')\cdot(\nabla u') + (\nabla v')\cdot(\nabla v') + (\nabla w')\cdot(\nabla w')}^{x,y}\right\}. \qquad (3.11)$$

The first term of the right-hand side represents the production of E from vertical shear of the mean currents, $\hat{\boldsymbol{u}}^{x,y} = \boldsymbol{u}_{\rm tide} + \overline{\boldsymbol{u}}^{x,y}$ (P-term), the second the vertical redistribution of E (R-term), and the third the dissipation of E due to viscosity (V-term).

Figure 11 shows the time-averaged vertical profiles of the P-term and R-term normalized by the outer scales, i.e. P-term$^- =$ P-term$/(u_\tau^2/T)$ and R-term$^-$ = R-term$/(u_\tau^2/T)$. P-term$^-$ was larger than R-term$^-$ for $z^- < 0.5$, but R-term$^-$ was large than P-term$^-$ for $z^- > 0.5$. This means that, for $z^- > 0.5$, perturbations were not generated locally by P-term$^-$, but transported from the bottom boundary layer by R-term$^-$. The upward transport became larger as Ro_t approached unity (cases C,D > B,E > A,F > Ek). This clearly explains the difference in q^- for $z^- > 0.5$ (figure 10*a*).

Figure 12 shows the time evolution of the horizontally averaged eddy kinetic energy $\overline{E}^{-x,y} = \overline{E}^{x,y}/u_\tau^2$ for cases A and D. In case D (figure 12*b*), it was clear that $\overline{E}^{-x,y}$ generated near the bottom propagated upward at almost constant speed in the form

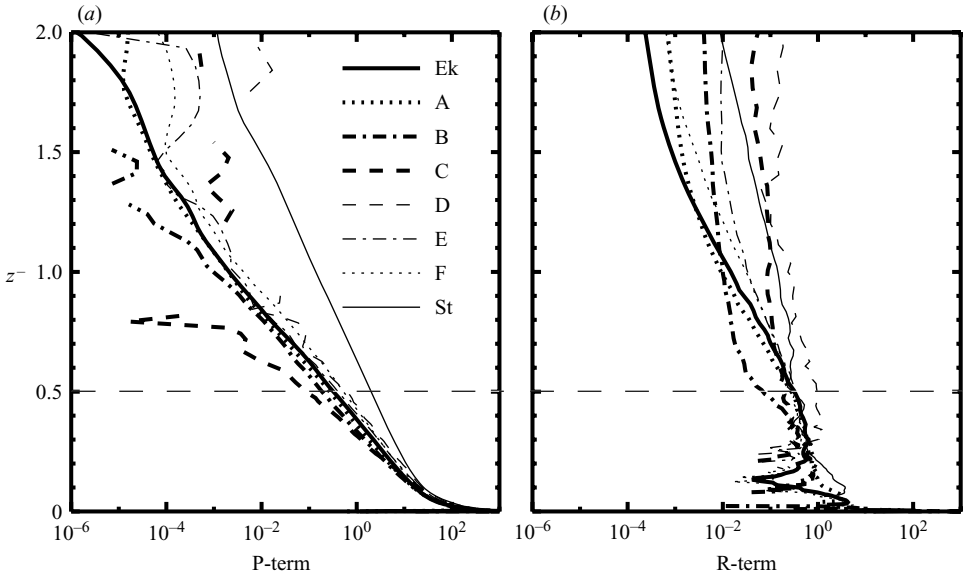

FIGURE 11. The vertical profiles of the production and redistribution terms (P- and R-terms) in the E-equation (3.11). The values are averaged horizontally and temporally, and normalized by the outer scale, u_τ^2/T.

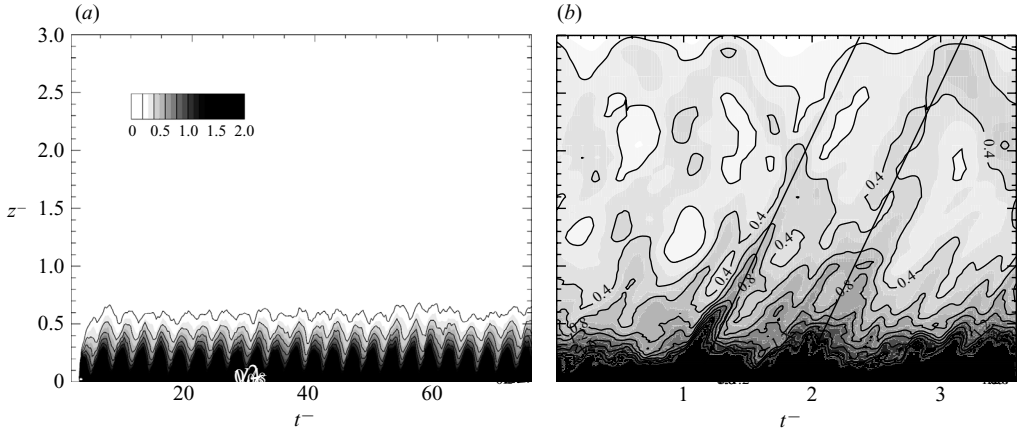

FIGURE 12. Time-evolution of $\overline{E^-}^{x,y}$ for (*a*) case A and (*b*) D. Both the time and vertical axes are normalized by the outer scales, T and δ, respectively. Contour interval is 0.2, and darker shades represent larger values. The two straight thick lines in (*b*) indicate the vertical phase velocity of inertial waves, $c_{pz}^- = 2.2$, given by (3.12). The oscillation of $\overline{E^-}^{x,y}$ in (*a*) is due to the tidal current oscillation.

of energy beams (reflection at the surface of $z^- = 3.0$ was also found). The travelling speed of the energy was approximately 2.1 in u_τ^* units.

Inertial waves (called gyroscopic waves in LeBlond & Mysak 1978) could be a candidate for the dynamical process inducing such energy propagation. The vertical phase velocity $|c_{pz}^-|$ of inertial waves with frequency ω^* and horizontal wavelength δ^*

case	Ek	A	B	C	D	E	F	St
Ro_t	0	0.5	0.8	0.95	1.05	1.2	2.0	∞
L^-_{decay}	–	0.682	12.7	204	207	16.8	–	–
T^-_{decay}	–	4.66	24.1	91.0	92.4	31.8	–	–
c^-_{gz}	–	0.146	0.529	2.24	2.24	0.529	–	–

TABLE 2. Length and time scales of dissipation and the vertical group velocity for the inertial waves with frequency ω^* of $1/T^*$ and horizontal wavelength λ^* of δ^*. The dash means that the waves cannot exist.

is given by (see Appendix C)

$$|c^-_{pz}| = \frac{|f^*T^*|(\lambda^*/\delta^*)}{2\pi\sqrt{2+2(\omega^*T^*)^2/((f^*T^*)^2-(\omega^*T^*)^2)}}. \tag{3.12}$$

Using $\omega^* = 1/T^*$ and $\lambda^* = \delta^*$ as representative perturbations of the turbulent boundary layer (e.g. Tennekes & Lumley 1972) (and $|f^*T^*| = 1/|1 - Ro| = 20$), (3.12) yields $|c^-_{pz}| = 2.2$ in u^*_τ units. This value agrees well with the experimental result, ~ 2.1. Together with the fact that the velocity components of the perturbation satisfied the phase relation of inertial waves (not shown), it can be concluded that upward transport of E by inertial waves caused intensification of q^- for $z^- > 0.5$ in cases with Ro_t close to unity (figure 10*a*). In contrast, propagation of inertial waves was unclear and $\overline{E^-}^{x,y}$ decreased rapidly to less than 0.2 at $z^- = 0.6$ in case A (figure 12*a*). Inertial waves also explain the suppression of l^- (figure 10*b*), since they can cause the upward transport of small-scale perturbations generated at lower levels.

Intensified inertial waves at Ro_t close to unity can be explained as follows. First, inertial waves with $\omega^* = 1/T^*$ and $\lambda^* = \delta^*$ can exist in five cases A to E, since the necessary condition for the wave excitation $\omega^* < |f^*|$ is satisfied. For these cases, viscosity acts to dissipate inertial waves during their propagation. The height which inertial waves reach before being dissipated, $L^-_{\mathrm{decay}} = L^*_{\mathrm{decay}}/\delta^*$, is estimated by (Appendix C)

$$L^-_{\mathrm{decay}} = |c^-_{gz}|T^-_{\mathrm{decay}}, \tag{3.13}$$

where $|c^-_{gz}|$ is the vertical group velocity given by

$$|c^-_{gz}| = \frac{|f^*T^*|(\lambda^*/\delta^*)}{2\pi\sqrt{2+2(\omega^*T^*)^2/((f^*T^*)^2-(\omega^*T^*)^2)}}\left(1-\frac{(\omega^*T^*)^2}{(f^*T^*)^2}\right), \tag{3.14}$$

and T^-_{decay} is the time scale of dissipation given by

$$T^-_{\mathrm{decay}} = \frac{(\lambda^*/\delta^*)^2}{8\pi^2\sqrt{2+2(\omega^*T^*)^2/((f^*T^*)^2-(\omega^*T^*)^2)}}\frac{T^*u^{*2}_\tau}{\nu^*}. \tag{3.15}$$

Table 2 shows L^-_{decay}, $|c^-_{gz}|$ and T^-_{decay} for the waves with $\omega^* = 1/T^*$ and $\lambda^* = \delta^*$ (the values of $|f^*T^*| = 1/|1 - Ro|$ and $T^*u^{*2}_\tau/\nu^* = ReTu^2_\tau$ in (3.14) and (3.15) were calculated from table 1). L^-_{decay} increased sharply as Ro_t approaches unity, from ~ 0.7 for case A to more than 200 for cases C and D. This dependence of L^-_{decay} on Ro_t explains the results in figure 10 (q^- and l^-) and figure 11(*b*) (R-term$^-$).

The increase of L^-_{decay} is attributed to an increase in both c^-_{gz} and T^-_{decay} as Ro_t approaches unity. Since the time scale $T^*(= 1/|f^* + \sigma^*|)$ increases compared to the inertial period $(1/|f^*|)$ as Ro_t approaches unity, f^*T^* which appears in (3.14)

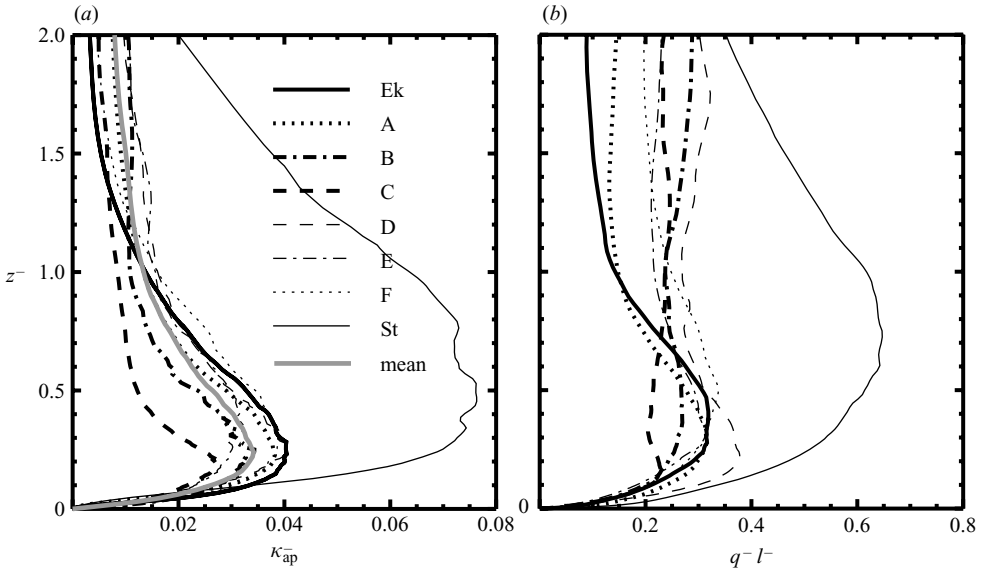

FIGURE 13. The normalized vertical profiles of (*a*) the apparent diffusivity $\kappa^-_{ap} = \kappa^*_{ap}/u^*_\tau \delta^*$ evaluated by (3.16) and (*b*) the product of the velocity and length scales, $q^- l^-$. The grey line in (*a*) indicates the averaged profile of cases A to F.

becomes large and acts to increase c^-_{gz}. Physically this means relative enhancement of the Coriolis effect compared to the oscillating effect. Since T^-_{decay} depends mainly on $T^* u^{*2}_\tau/\nu^*$ in (3.15), the increased T^* makes T^-_{decay} larger. This is interpreted as a reduction of the viscous effect due to the large length scale (wavelength) $\delta^* = T^* u^*_\tau$.

3.4. *Turbulent mixing*

We evaluated the effect of turbulent mixing based on the experimental results. Since stratification was not considered in this study, energy conversion from turbulent motion to potential energy did not occur. Therefore, the mixing effect shown here provides an upper bound of that in actual oceans. For evaluation of the mixing effect, the time-evolution of passive tracer C was calculated by integrating temporally the non-dimensional advection–diffusion equation (the diffusivity was set equal to the viscosity) using the obtained velocity field. The initial distribution of the tracer was given by $C = z$. Based on the calculated tracer distribution, an apparent diffusivity κ_{ap} was estimated by

$$-\kappa_{ap} \frac{\mathrm{d}\overline{C}^{x,y,t}}{\mathrm{d}z} = \overline{w'C'}^{x,y,t}, \tag{3.16}$$

where $C' = C - \overline{C}^{x,y}$. Figure 13(*a*) shows the vertical profile of the apparent diffusivity normalized by the outer scales, $\kappa^-_{ap} (= \kappa^*_{ap}/u^*_\tau \delta^* = \kappa_{ap}/u_\tau \delta)$. The profile of κ^-_{ap} was similar among cases A to F and case Ek (relatively small in case C). It reached maxima of 0.035 to 0.040 at $z^- \sim 0.3$, and decreased with height to $\sim$0.01 at $z^- = 1.0$.

Turbulent diffusivity is theoretically proportional to the velocity and length scales, q and l (e.g. Tennekes & Lumley 1972). Figure 13(*b*) shows the normalized product, $q^- l^-$, based on the results in figure 10. As expected from the vertical profiles of q^- and l^- in figure 10, similarity in $q^- l^-$ was not clear especially for $z^- > 0.5$. Since κ^-_{ap} showed good similarity while $q^- l^-$ did not, it is suggested that inertial waves make

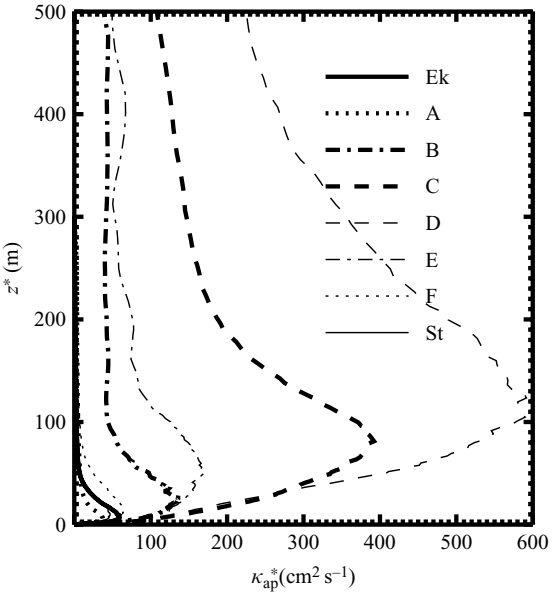

FIGURE 14. As figure 13(*a*), but with dimensional variables for $\sigma^* = 1.4 \times 10^{-4}\,\mathrm{s}^{-1}$ (M2-tide), $U^*_{\mathrm{tide}} = 8.4\,\mathrm{cm\,s}^{-1}$ and $\nu^* = 1.0\,\mathrm{cm}^2\,\mathrm{s}^{-1}$.

little contribution to tracer mixing. In fact, strong mixing did not occur in cases C and D where inertial waves were active (e.g. figure 12*b*). One possible reason is that wave breaking may have not occurred at low Reynolds numbers (~ 4500). A similar result was shown by Iida, Kasagi & Nagano (2002) who studied a turbulent boundary layer in a stably stratified fluid with Reynolds number ~ 5000. They reported that mixing was much weaker in the region dominated by waves (internal waves) than by turbulence, though the strength and length of perturbations were the same in both regions. For higher *Re*, inertial waves (or internal waves in the stratified fluid) may intensify mixing through their shear instability.

The similarity in κ^-_{ap} suggests that the dimensional turbulent diffusivity κ^*_{ap} in the TBBL is given by a function of the Coriolis parameter (f^*), the tidal frequency (σ^*) and the tidal amplitude (U^*_{tide}),

$$\kappa^*_{\mathrm{ap}}(z^*) = u^*_\tau \delta^* \mathscr{K}(z^*/\delta^*), \tag{3.17}$$

where

$$u^*_\tau = C_\tau U^*_{\mathrm{tide}} \qquad \text{and} \qquad \delta^* = u^*_\tau / |f^* + \sigma^*|. \tag{3.18}$$

The coefficient $C_\tau = u^*_\tau / U^*_{\mathrm{tide}} = u_\tau$ was estimated at ~ 0.04 as shown in table 1. The function $\mathscr{K}$ in (3.17) denotes the non-dimensional universal structure of κ^*_{ap}. The averaged profile of κ^-_{ap} from cases A to F (the grey line in figure 13*a*) may serve as a possible function for $\mathscr{K}$, although more experimental cases are needed to improve its reliability.

Dependence of κ^*_{ap} on δ^* implies two important features of κ^*_{ap} in the actual ocean. First, the magnitude of κ^*_{ap} increases as the critical latitude becomes closer, $|f^*| \sim |\sigma^*|$, even if the tidal amplitude (or u^*_τ) is unchanged. Second, the vertical region over which κ^*_{ap} is significant becomes wider as well. As seen in figure 14, the maximum value of κ^*_{ap} increased from $60\,\mathrm{cm}^2\,\mathrm{s}^{-1}$ in case F ($\delta^* = 34\,\mathrm{m}$) to $600\,\mathrm{cm}^2\,\mathrm{s}^{-1}$ in case D ($\delta^* = 460\,\mathrm{m}$).

The height at which κ^*_{ap} has a maximum value also increased from 11 m in case F to 130 m in case D.

4. Conclusions and discussion

To investigate turbulent properties of the tidally induced bottom boundary layer (TBBL) in a rotating frame, we conducted three-dimensional direct numerical simulations under unstratified conditions for eight cases, varying the temporal Rossby number, $Ro_t = |\sigma^*/f^*|$, the ratio of the tidal frequency σ^* and the Coriolis parameter f^*.

Introducing new modified outer scales, the velocity scale u^*_τ (frictional velocity), the time scale $T^* = 1/|f^* + \sigma^*|$ and the length scale $\delta^* = u^*_\tau/|f^* + \sigma^*|$ (σ^* is positive when the tidal ellipse rotates anticlockwise), we confirmed that turbulent properties are explained well by these scales. The velocity defects and horizontal stresses showed good similarity and coincided well with those in the turbulent Ekman layer (Tennekes & Lumley 1972; Coleman 1999), and the thickness of the TBBL was given by δ^* regardless of Ro_t. This implies that the similarity of the turbulent Ekman layer is universally applicable to the TBBL in the worlds oceans except at the equator. The results obtained here are quite different from those based on laminar flow (or a flow with assumed constant viscosity ν^*), for which the vertical scale of the TBBL is $H^*_{tide} = \sqrt{2\nu^*/|f^* + \sigma^*|}$ (e.g. Prandle 1982; Furevik & Foldvik 1996). In units of H^*_{tide} the thickness of the TBBL changed from 20 to 50 depending on Ro_t.

The tracer experiments showed that the magnitude and vertical profile of the apparent diffusivity κ^*_{ap} have similarity again when normalized by the outer scales. This implies that the diffusivity κ^*_{ap} can be represented by a universal function of the latitude (f^*), the tidal frequency (σ^*) and amplitude (u^*_τ), such as (3.17).

Inertial waves were excited by turbulence and attenuation of inertial waves due to viscosity was weak when Ro_t approached unity. As a result, the perturbation field deviated from similarity when $Ro_t \sim 1$. However, the inertial waves made little contribution to the mixing processes, probably because wave breaking did not occur at low Reynolds numbers in the present experiments (1000–4500).

It is worth discussing the applicability of the present results to actual situations although some factors affecting turbulent properties such as stratification and bottom topography were excluded in the experiments and quantitative estimation is not easy. Werner *et al.* (2003) made detailed observations on Georges Bank (41° N) and modelled investigations with an assumed eddy viscosity and a turbulent closure scheme (Mellor & Yamada 1982). In winter, the M2 tidal current with amplitude of 30∼40 cm s^{-1} showed a significant vertical shear 20 ∼ 30 m above the bottom, and a well-mixed layer was established. The height of the shear layer, 20∼30 m, is roughly a tenth of $\delta^* \sim 300$ m which is evaluated with $u^*_\tau \sim 1.4$ cm s^{-1}. The eddy viscosity estimated by the turbulent closure scheme exceeded 200 cm^{2}s^{-1} (450 cm^2 s^{-1} maximum at the height of 20 m) in the whole water depth except the upper and lower boundaries. These features are consistent with our results in figures 8 and 13 although the water depth is much shallower than the outer scale δ^*.

Near the M2 critical latitude (74.5° N) in the Barents Sea, it has been documented that the M2 tidal current has a vertical shear over almost the whole water depth of 300 ∼ 400 m (Nøst 1994; Furevik & Foldvik 1996). Similar thick shear layers have also been observed in the M2 current profiles on the southern shelf of the Weddell Sea (∼74°S) (Foldvik *et al.* 1990; Makinson *et al.* 2006). In these regions, δ^* becomes several thousand metres or more, as the whole water layer is probably included in

the strong shear layer with a thickness of $0.1\delta^* \sim 0.2\delta^*$. Even though vertical shear of the tidal currents is concentrated below $0.1\delta^*$ (figure 8), $0.1\delta^*$ m is large enough to explain the observations of the thick TBBL. Nøst (1994) has tried to reproduce the observed profile of the tidal current using a one-dimensional model with several assumed profiles of eddy viscosity, and obtained a better result when a parabolic profile which resembles the similar profile of κ_{ap} (figure 13) is assumed. This implies that the properties of a turbulent TBBL obtained here may mainly act to determine features of tidal phenomena in the actual situation.

From this viewpoint, the similarity in the mixing effect would be valuable for modification of bottom mixing parameterizations used in large-scale models. In the experiments, the turbulent diffusivity κ^*_{ap} was proportional to $u^*_\tau\delta^*$, and the vertical extent of the active mixing region to δ^* as indicated by (3.17). This means that mixing parameterizations should depend on f^* and σ^* as well as the amplitude of the tidal currents (u^*_τ), so that strong mixing occurs near the critical latitude. Such modification is expected to be effective to improve the total performance of large-scale models, since reproducing the formation process of the bottom water in polar oceans is important for global thermohaline circulation (e.g. Nakano & Suginohara 2002).

For diurnal tides, a thick turbulent TBBL is possible near the latitude of 30° (e.g. Craig 1989), and the similarity obtained here serves as a basis for understanding its effect on mixing processes. On the other hand, factors neglected here should be examined in future for quantitative estimation. First, stratification should be taken into account, since stratification strongly affects turbulent characteristics and the mixing processes as indicated by studies on the nocturnal atmosphere boundary layer (Nieuwstadt 1984; Basu *et al.* 2006). We examine the basic features of the TBBL under a stratified condition in a companion paper (Sakamoto & Akitomo 2008). The terrain in the real oceans modifies the pressure gradient and complicates the tidal ellipses. Furthermore, interaction of many tidal constituents may modify turbulent characteristics, although only a single constituent was considered here. The model basin used here was deep enough (more than $3\delta^*$) to avoid the influence of the sea surface. However, when δ^* exceeds the water depth, the sea surface should be considered, since water depth may be a more appropriate scaling factor for the outer length (e.g. Tennekes & Lumley 1972). The low Reynolds numbers Re of the experiments, ranging from 1000 to 4500, limits the applicability to the real ocean with typical Re values of $\sim 10^6$. For high Re, strong inertial waves which appeared at Ro_t close to unity may intensify the mixing effect through wave breaking.

Despite these restrictions, the similarity obtained here provides a basis for universal understanding of the turbulent TBBL under the Earth's rotation.

The authors wish to express their thanks to Professor T. Awaji, Assistant Professor M. Konda and Assistant Professor Y. Ishikawa for helpful discussions throughout this study. Numerical calculations were carried out on PRIMEPOWER HPC2500 at the Academic Center for Computing and Media Studies of Kyoto University.

Appendix A. The effect of the horizontal component of the Earth's rotation

An additional experiment under the same conditions as in case F ($Ro_t = 2.0$) but using $(\boldsymbol{f} \times \boldsymbol{u})/Ro$ instead of $(\boldsymbol{z} \times \boldsymbol{u})/Ro$ in (2.6*a*), where $\boldsymbol{f} = (0, \tan\phi, 1)$ ($\phi = 30°$: latitude), was done to examine the effect of the horizontal component of the Earth's rotation vector (called case F′).

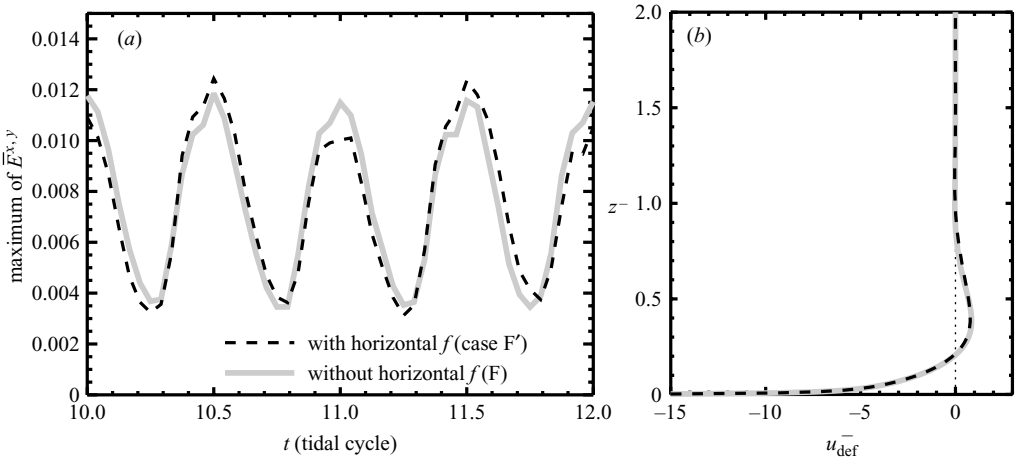

FIGURE 15. (*a*) Time evolution of the maximum value of $\overline{E}^{x,y}$ and (*b*) the vertical profile of the time-averaged velocity defects, $\overline{\overline{u}^-_{\rm def}}^{x,y,t}$. Grey solid (black dashed) lines indicate case F (case F′).

Figure 15(*a*) compares the time evolution of the eddy kinetic energy $\overline{E}^{x,y}$ between cases F and F′. In case F′, the horizontal component of the Earth's rotation intensified turbulence when $\boldsymbol{u}_{\rm int}$ was westward ($t = 10.5$ and 11.5), but weakened it when eastward ($t = 10.0$, 11.0 and 12.0), and this dependence on the direction of the interior flow is consistent with Coleman *et al.* (1990).

Despite the discrepancy in the tidal cycle between cases F and F′, turbulent statistics averaged temporally over a tidal period were hardly changed. The differences of the time-mean $\overline{E}^{x,y,t}$ and the bottom stress $\overline{\tau_b}^{x,y,t}$ were below 1.0 % and 0.8 %, respectively. The vertical profiles of the velocity defect were almost identical for cases F and F′ (figure 15*b*). This is because the differences were cancelled out over a tidal cycle. In conclusion, the horizontal component of the Earth's rotation vector has little influence on turbulent statistics averaged over a tidal cycle, which are of primary concern in this study.

Appendix B. Energy spectra and velocity profiles in the boundary layer

In the present experiments, the energy spectrum and the vertical profile of velocity in the boundary layer showed good agreement with the turbulent theory by Tennekes & Lumley (1972).

According to Tennekes & Lumley (1972), for anisotropic and homogeneous turbulence, the three-dimensional energy spectrum, which is the kinetic energy of perturbations with the wavenumber $k^* = |\boldsymbol{k}^*|$ (where $\boldsymbol{k}^* = (k^*_x, k^*_y, k^*_z)$ is the wavenumber vector), has the following profile $\mathscr{E}^*_{\rm the}(k^*)$ in the high wavenumber region:

$$\mathscr{E}^*_{\rm the}(k^*) = \alpha {\epsilon^*}^{2/3} {k^*}^{-5/3} \exp\left(-\tfrac{3}{2}\alpha(\eta^* k^*)^{4/3}\right), \tag{B 1}$$

where $\alpha = 1.5$, $\epsilon^* = \nu^*((\nabla u)^2 + (\nabla v)^2 + (\nabla w)^2)$ and $\eta^* = ({\nu^*}^3/\epsilon^*)^{1/4}$ are the empirical constant, the rate of viscous dissipation and the Kolmogorov scale, respectively. On the other hand, the three-dimensional energy spectrum can be directly estimated from

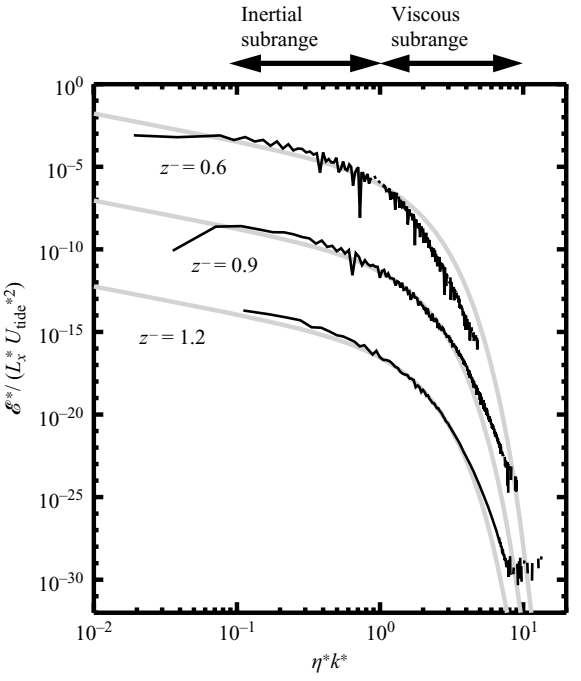

FIGURE 16. Three-dimensional energy spectra $\mathscr{E}^{*}_{\mathrm{exp}}(k^{*})$ estimated by (B 2) (black lines) and $\mathscr{E}^{*}_{\mathrm{the}}(k^{*})$ given by (B 1) (grey lines) at $z^{-} = 0.6, 0.9$ and 1.2 for case A. The energy spectra and the wavenumber are normalized by $L_x^{*} U_{\mathrm{tide}}^{*\,2}$ and η^{*}, respectively, and the profiles show the spectra averaged over t^{*} and y^{*}. Note that the profiles at $z^{-} = 0.9$ and 1.2 are offset by 10^{-5} and 10^{-10}, respectively.

the velocity field of the experimental results by means of

$$\mathscr{E}^{*}_{\mathrm{exp}}(k^{*}) = k^{*3} \frac{\mathrm{d}}{\mathrm{d}k^{*}} \left(\frac{1}{k^{*}} \frac{\mathrm{d}\mathscr{S}^{*}(k^{*})}{\mathrm{d}k^{*}} \right), \tag{B 2}$$

where $\mathscr{S}^{*}$ is the x-direction one-dimensional spectrum of u^{*} (Tennekes & Lumley 1972). As seen in figure 16, $\mathscr{E}^{*}_{\mathrm{exp}}$ coincided with $\mathscr{E}^{*}_{\mathrm{the}}$ for the high wavenumber region, $\eta^{*}k^{*} > 0.1$, that is, $\mathscr{E}^{*}_{\mathrm{exp}} \propto k^{*-5/3}$ for $0.1 < \eta^{*}k^{*} < 1$ (the inertial subrange), and $\mathscr{E}^{*}_{\mathrm{exp}}$ drops sharply for $\eta^{*}k^{*} > 1$ (the viscous subrange).

It has also been revealed that the horizontal velocity in the turbulent boundary layer has a universal profile near the boundary (Tennekes & Lumley 1972). In the form normalized by the frictional velocity u^{*}_{τ} and the length scale ν^{*}/u^{*}_{τ}, the vertical profile of the horizontal velocity is given by

$$\mathscr{U}^{*}_{\mathrm{the}}(z^{*})/u^{*}_{\tau} = z^{*}/(\nu^{*}/u^{*}_{\tau}), \tag{B 3}$$

in the viscous sublayer with $z^{*}/(\nu^{*}/u^{*}_{\tau}) < 5$, and

$$\mathscr{U}^{*}_{\mathrm{the}}(z^{*})/u^{*}_{\tau} = 2.5 \ln(z^{*}/(\nu^{*}/u^{*}_{\tau})) + 5, \tag{B 4}$$

in the logarithmic sublayer with $z^{*}/(\nu^{*}/u^{*}_{\tau}) > 30$ (its upper limit depends on the Reynolds number). Between the two layers ($5 < z^{*}/(\nu^{*}/u^{*}_{\tau}) < 30$), the profiles are connected smoothly with each other. Figure 17 shows $\mathscr{U}^{*}_{\mathrm{the}}$ and the corresponding velocity profile of the experimental results $\mathscr{U}^{*}_{\mathrm{exp}}$. ($\mathscr{U}^{*}_{\mathrm{exp}}$ is the averaged velocity component parallel to the bottom stress vector, that is, $\mathscr{U}^{*}_{\mathrm{exp}}(z^{*}) =$

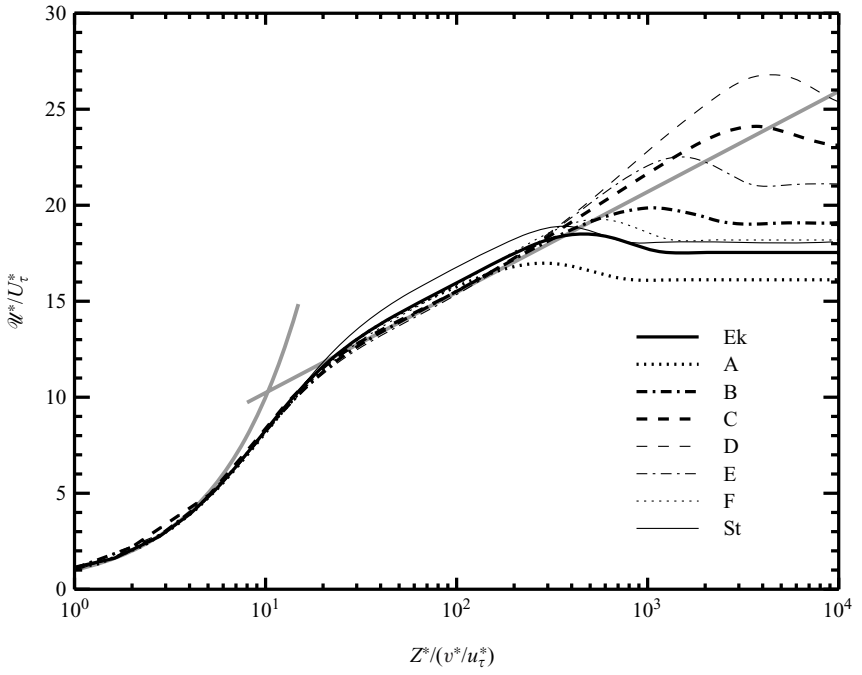

FIGURE 17. The vertical profiles of $\mathscr{U}^*_{\rm exp}$ for all eight cases and $\mathscr{U}^*_{\rm the}$ given by (B 3) and (B 4) (grey lines). The horizontal and vertical axes denote the normalized height $z^*/(\nu^*/u^*_\tau)$ and the normalized velocity $\mathscr{U}^*_{\rm exp}/u^*_\tau$ (or $\mathscr{U}^*_{\rm the}/u^*_\tau$), respectively.

$\overline{\hat{u}^* \cos\theta_{\rm btm} + \hat{v}^* \sin\theta_{\rm btm}}^{x^*,y^*,t^*}$, where $\theta_{\rm btm}(t^*)$ is the azimuthal angle of the bottom stress.) For all cases, $\mathscr{U}^*_{\rm exp}$ exhibited good agreement with $\mathscr{U}^*_{\rm the}$ (the upper limit of the logarithmic sublayer changed from $z^*/(\nu^*/u^*_\tau) \sim 200$ to 500).

Here, we summarize the model resolution and the domain size in units of the length scales for the turbulent boundary layer. The horizontal grid interval $\Delta x^*(= \Delta y^*)$ is in the range from 4.4 (case St) to 21 (D) and the minimum of the vertical one Δz^* is from 0.70 (St) to 3.4 (D) in units of ν^*/u^*_τ. The horizontal domain size $L^*_x(= L^*_y)$ is from 0.75 (case D) to 3.7 (St) and the vertical one H^* is from 3.0 (D) to 15 (St) in units of the outer length scale δ^*.

Appendix C. Inertial waves and their decay scales

Consider inertial waves excited in an inviscid homogeneous fluid of the unbounded region. Based on the linear theory (Friedlander 1980, Chap. 7), the dispersion relation of an inertial wave is given by

$$\omega^* = \pm \frac{k^*_z}{|\boldsymbol{k}^*|} f^*, \tag{C 1}$$

in a dimensional form, where ω^* and f^* are the wave angular frequency and the Coriolis parameter, and $\boldsymbol{k}^* = (k^*_x, k^*_y, k^*_z)$ is the wavenumber vector. Thus, inertial waves having horizontal structure $(k^*_x, k^*_y \neq 0)$ can be excited when $|\omega^*| < |f^*|$.

Here, we estimate the height which inertial waves excited at the bottom reach in a viscous fluid. For inertial waves having horizontal wavelength λ^* $(k^*_x = k^*_y = 2\pi/\lambda^*)$,

$|\boldsymbol{k}^*|$ is given by

$$|\boldsymbol{k}^*| = \frac{2\pi}{\lambda^*}\sqrt{2 + 2\omega^{*2}/(f^{*2} - \omega^{*2})}, \tag{C 2}$$

with the aid of (C 1). Then, the vertical phase and group velocities, c^*_{pz} and c^*_{gz}, are expressed by

$$c^*_{pz} = \frac{\omega^*}{k^*_z} = \pm\frac{f^*}{|\boldsymbol{k}^*|} = \pm\frac{f^*\lambda^*}{2\pi\sqrt{2 + 2\omega^{*2}/(f^{*2} - \omega^{*2})}}, \tag{C 3}$$

$$c^*_{gz} = \frac{\partial\omega^*}{\partial k^*_z} = \pm\frac{f^*}{|\boldsymbol{k}^*|}\left(1 - \frac{\omega^{*2}}{f^{*2}}\right) = \pm\frac{f^*\lambda^*}{2\pi\sqrt{2 + 2\omega^{*2}/(f^{*2} - \omega^{*2})}}\left(1 - \frac{\omega^{*2}}{f^{*2}}\right). \tag{C 4}$$

When normalized by the outer scales, i.e. the velocity scale u^*_τ, the time scale T^* and the length scale $\delta^* = u^*_\tau T^*$, these velocities are written as

$$c^-_{pz} = \pm\frac{(f^*T^*)(\lambda^*/\delta^*)}{2\pi\sqrt{2 + 2(\omega^*T^*)^2/((f^*T^*)^2 - (\omega^*T^*)^2)}}, \tag{C 5}$$

$$c^-_{gz} = \pm\frac{(f^*T^*)(\lambda^*/\delta^*)}{2\pi\sqrt{2 + 2(\omega^*T^*)^2/((f^*T^*)^2 - (\omega^*T^*)^2)}}\left(1 - \frac{(\omega^*T^*)^2}{(f^*T^*)^2}\right). \tag{C 6}$$

After a sufficient lapse of time, the upward energy transfer due to waves balances the dissipation due to viscosity at any height. That is,

$$\frac{\partial}{\partial z^*}\left(c^*_{gz}\overline{E^*}^{x^*,y^*}\right) = \nu^*\overline{\nabla^2 E^*}^{x^*,y^*}, \tag{C 7}$$

where $E^* = (u^{*2} + v^{*2} + w^{*2})/2$ is the kinetic energy of waves, ν^* the viscosity, ∇^2 the Laplacian operator, and the overbar denotes the horizontal average. Since the dissipation term $\nu^*\overline{\nabla^2 E^*}^{x^*,y^*}$ is rewritten as $2\nu^*|\boldsymbol{k}^*|^2\overline{E^*}^{x^*,y^*}$ and c^*_{gz} is independent of z^*, (C 7) becomes

$$c^*_{gz}\frac{\partial}{\partial z^*}\overline{E^*}^{x^*,y^*} = 2\nu^*|\boldsymbol{k}^*|^2\overline{E^*}^{x^*,y^*}. \tag{C 8}$$

Then, the solution of (C 8) is obtained as

$$\overline{E^*}^{x^*,y^*}(z^*) = \overline{E^*}^{x^*,y^*}(0)\exp\left(-\frac{z^*}{L^*_{\mathrm{decay}}}\right), \tag{C 9}$$

where $\overline{E^*}^{x^*,y^*}(0)$ is the wave energy supplied at the bottom, and L^*_{decay}, representing the height to which inertial waves propagate before being dissipated, is

$$L^*_{\mathrm{decay}} = \frac{|c^*_{gz}|}{2|\boldsymbol{k}^*|^2\nu^*}. \tag{C 10}$$

Thus, L^*_{decay} can be interpreted as a product of the group velocity $|c^*_{gz}|$ and the time scale $T^*_{\mathrm{decay}} = 1/(2|\boldsymbol{k}^*|^2\nu^*)$. In the normalized form, T^-_{decay} and L^-_{decay} are written

$$T^-_{\mathrm{decay}} = \frac{(\lambda^*/\delta^*)^2}{8\pi^2\sqrt{2 + 2(\omega^*T^*)^2/((f^*T^*)^2 - (\omega^*T^*)^2)}}\frac{T^*u^{*2}_\tau}{\nu^*}, \tag{C 11}$$

$$L^-_{\mathrm{decay}} = |c^-_{gz}|T^-_{\mathrm{decay}}. \tag{C 12}$$

REFERENCES

Aelbrecht, D., D'Hieres, G. C. & Renouard, D. 1999 Experimental study of the Ekman layer instability in steady or oscillating flows. *Continental Shelf Res.* **19**, 1851–1867.

Akhavan, R., Kamm, R. D. & Shapiro, A. H. 1991*a* An investigation of transition to turbulence in bounded oscillatory Stokes flows. Part 1. Experiments. *J. Fluid Mech.* **225**, 395–422.

Akhavan, R., Kamm, R. D. & Shapiro, A. H. 1991*b* An investigation of transition to turbulence in bounded oscillatory Stokes flows. Part 2. Numerical simulations. *J. Fluid Mech.* **225**, 423–444.

Akitomo, K. 1999 Open-ocean deep convection due to thermobaricity 2. Numerical experiments. *J. Geophys. Res.* **104**, 5235–5249.

Basu, S., Porté-Agel, F., Foufoula-Georgiou, E., Vinuesa, J.-F. & Pahlow, M. 2006 Revisiting the local scaling hypothesis in stably stratified atmospheric boundary-layer turbulence: An integration of field and laboratory measurements with large-eddy simulations. *Boundary-Layer Met.* **119**, 473–500.

Coleman, G. N. 1999 Similarity statistics from a direct numerical simulation of the neutrally stratified planetary boundary layer. *J. Atmos. Sci.* **56**, 891–900.

Coleman, G. N., Ferziger, J. H. & Spalart, P. R. 1990 A numerical study of the turbulent Ekman layer. *J. Fluid Mech.* **213**, 313–348.

Coleman, G. N., Ferziger, J. H. & Spalart, P. R. 1992 Direct simulation of the stably stratified turbulent Ekman layer. *J. Fluid Mech.* **244**, 677–712.

Coles, D. 1956 The law of the wake in the turbulent boundary layer. *J. Fluid Mech.* **1**, 191–226.

Costamagna, P., Vittori, G. & Blondeaux, P. 2003 Coherent structures in oscillatory boundary layers. *J. Fluid Mech.* **474**, 1–33.

Craig, P. D. 1989 A model of diurnally forced vertical current structure near 30° latitude. *Continental Shelf Res.* **9**, 965–980.

Csanady, G. T. 1967 On the "resistance law" of a turbulent Ekman layer. *J. Atmos. Sci.* **24**, 467–471.

Fahrbach, E., Harms, S., Rohardt, G., Schröder, M. & Woodgate, R. A. 2001 Flow of bottom water in the northwestern Weddell Sea. *J. Geophys. Res.* **106**, 2761–2778.

Fahrbach, E., Rohardt, G., Scheele, N., Schröder, M., Strass, V. & Wisotzki, A. 1995 Formation and discharge of deep and bottom water in the northwestern Weddell Sea. *J. Mar. Res.* **53**, 515–538.

Faller, A. J. & Kaylor, R. E. 1966 A numerical study of the instability of the laminar Ekman boundary layer. *J. Atmos. Sci.* **23**, 466–480.

Foldvik, A., Gammelsrød, T., Østerhus, S., Fahrbach, E., Rohardt, G., Schröder, M., Nicholls, K. W., Padman, L. & Woodgate, R. A. 2004 Ice shelf water overflow and bottom water formation in the southern Weddell Sea. *J. Geophys. Res.* **109**, C02015.

Foldvik, A., Middleton, J. H., Foster, T. D. 1990 The tides of the southern Weddell Sea. *Deep-Sea Res.* **37**, 1345–1362.

Foster, T. D. & Carmack, E. C. 1976 Frontal zone mixing and Antarctic Bottom Water formation in the southern Weddell Sea. *Deep-Sea Res.* **23**, 301–317.

Foster, T. D., Foldvik, A. & Middleton, J. H. 1987 Mixing and bottom water formation in the shelf break region of the southern Weddell Sea. *Deep-Sea Res.* **34**, 1771–1794.

Friedlander, S. 1980 *An Introduction to the Mathematical Theory of Geophysical Fluid Dynamics.* Elsevier.

Furevik, T. & Foldvik, A. 1996 Stability at M(2) critical latitude in the Barents Sea. *J. Geophys. Res.* **101**, 8823–8837.

Gordon, A. L. 1998 Western Weddell Sea thermohaline stratification. Ocean, ice and atmosphere: Interactions at the Antarctic continental margin. *Antarct. Res. Ser.* **75**, 215–240.

Grant, W. D. & Madsen, O. S. 1986 The continental-shelf bottom boundary layer. *Annu. Rev. Fluid Mech.* **18**, 265–305.

Iida, O., Kasagi, N. & Nagano, Y. 2002 Direct numerical simulation of turbulent channel flow under stable density stratification. *Intl J. Heat Mass Transfer* **45**, 1693–1703.

Jacobs, S. S. 2004 Bottom water production and its links with the thermohaline circulation. *Antarct. Sci.* **16**, 427–437.

Kulikov, E. A., Rabinovich, A. B. 2004 Barotropic and baroclinic tidal currents on the Mackenzie shelf break in the southeastern Beaufort Sea. *J. Geophys. Res.* **109**, C05020.

LeBlond, P. H. & Mysak, L. A. 1978 *Waves in the Ocean.* Elsevier.

MAKINSON, K. 2002 Modeling tidal current profiles and vertical mixing beneath Filchner–Ronne Ice Shelf, Antarctica. *J. Phys. Oceanogr.* **32**, 202–215.

MAKINSON, K., SCHRÖDER, M. & ØSTERHUS, S. 2006 Effect of critical latitude and seasonal stratification on tidal current profiles along Ronne Ice Front, Antarctica. *J. Geophys. Res.* **111**, C03022.

MATSUNO, T. 1996 Numerical integrations of the primitive equations by a simulated backward difference method. *J. Met. Soc. Japan* **44**, 76–84.

MELLOR, G. L. & YAMADA, T. 1982 Development of a turbulence closure model for geophysical fluid problems. *Rev. Geophys. Space Phys.* **20**, 851–875.

MUENCH, R. D. & GORDON, A. L. 1995 Circulation and transport of water along the western Weddell Sea margin. *J. Geophys. Res.* **100**, 18503–18515.

NAKANO, H. & SUGINOHARA, N. 2002 Effects of Bottom Boundary Layer parameterization on reproducing deep and bottom waters in a world ocean model *J. Phys. Oceanogr.* **32**, 1209–1227.

NIEUWSTADT, F. T. M. 1984 The turbulent structure of the stable, nocturnal boundary layer. *J. Atmos. Sci.* **41**, 2202–2216.

NØST, E. 1994 Calculating tidal current profiles from vertically integrated models near the critical latitude in the Barents Sea. *J. Geophys. Res.* **99**, 7885–7901.

ORSI, A. H., JOHNSON, G. C. & BULLISTER, J. L. 1999 Circulation, mixing and production of Antarctic Bottom Water. *Progr. Oceanogr.* **43**, 55–109.

PEREIRA, F. P., BECKMANN, A. & HELLMER, H. H. 2002 Tidal mixing in the southern Weddell Sea: Results from a three-dimensional model. *J. Phys. Oceanogr.* **32**, 2151–2170.

PRANDLE, D. 1982 The vertical structure of tidal currents. *Geophys. Astrophys. Fluid Dyn.* **22**, 29–49.

ROBERTSON, R. 2001*a* Internal tides and baroclinicity in the southern Weddell Sea 1. Model description. *J. Geophys. Res.* **106**, 27001–27016.

ROBERTSON, R. 2001*b* Internal tides and baroclinicity in the southern Weddell Sea 2. Effects of the critical latitude and stratification. *J. Geophys. Res.* **106**, 27017–27034.

ROBERTSON, R., PADMAN, L. & EGBERT, G. D. 1998 Tides in the Weddell Sea. *Antarct. Res. Ser.* **75**, 341–369.

SAKAMOTO, K. & AKITOMO, K. 2006 Instabilities of the tidally induced bottom boundary layer in the rotating frame and their mixing effect. *Dyn. Atmos. Oceans* **41**, 191–211.

SAKAMOTO, K. & AKITOMO, K. 2008 The tidally induced bottom boundary layer in a rotating frame: Development of the turbulent mixed layer under stratification. *J. Fluid Mech.* (in press).

SCHMITZ, W. J. 1995 On the interbasin-scale thermohaline circulation. *Rev. Geophys.* **33**, 151–173.

SOULSBY, R. L. 1983 The bottom boundary layer of shelf seas. In *Physical Oceanography of Coastal and Shelf Seas* (ed. B. Johns), pp. 189–266. Elsevier.

SPALART, P. R. 1989 Theoretical and numerical study of a three-dimensional turbulent boundary layer. *J. Fluid Mech.* **205**, 319–340.

TENNEKES, H. & LUMLEY, J. L. 1972 *A First Course in Turbulence*. MIT Press.

WERNER, S. R., BEARDSLEY, R. C., LENTZ, S. J., HEBERT, D. L., OAKEY, N. S. 2003 Observations and modelling of the tidal bottom boundary layer on the souther flank of Georges Bank. *J. Geophys. Res.* **108**, 8005.

WHITE, M. 1994 Tidal and subtidal variability in the sloping benthic boundary layer. *J. Geophys. Res.* **99**, 7851–7864.

ZIKANOV, O., SLINN, D. N. & DHANAK, M. R. 2003 Large-eddy simulations of the wind-induced turbulent Ekman layer. *J. Fluid Mech.* **495**, 343–368.